

Chapter 2

Vitrified Bonding Systems and Heat Treatment

2.1 Vitrified Bonding Systems

Grinding wheels of various types, sizes, and shapes are geometrically defined bodies consisting of abrasive grains bonded with various types of ceramic bond. During heat treatment, or firing, the alumina and bonding minerals react with the bond, and this has an important effect on the properties of the resultant tool. For this reason, studies of the structure of abrasive tools made of alumina, and the determination of the phase composition and structure of their bonds are important research tasks. Generally speaking, grinding wheels are made in the following way. The bond materials are ground until they can pass through a 120 mesh screen without leaving a residue, weighed, and mixed. The firing resistance of the bond is checked and it is then passed to the press shop. Here, alumina of the required size and the bond materials are weighed in the quantities specified by the formulation, moistened with a dextrin or sodium silicate solution, and thoroughly mixed in a planetary mixer. The finished molding material is carefully weighed into exact portions that are then poured into moulds and compressed to the required volume. The molded product is then dried at 90–100°C and fired. Heat treatment, or firing, takes place at temperatures of 1,250–1,300°C, in continuous or batch furnaces. The relatively long firing times (up to 80–120 h) are due firstly to the nonuniformity of abrasive tools, composed of abrasive grain and ceramic bond, and secondly to the need for the bond to become sufficiently mobile to coat the abrasive grains without disturbing the structure of the tool or deforming it. Firing time and, more importantly, the length of time spent in the preheating and cooling zones of the kiln also depend on the dimensions of the abrasive tools, and increase with their size. Fired grinding wheels are machined on lathes to the required shape and size. Finished abrasive tools undergo hardness tests, and grinding wheels are additionally rupture tested at 1.5–2 times their peripheral velocity.

2.2 Grinding Wheel Structure Formation During Heat Treatment

Ceramic bond materials are made of refractory and fusible clays, feldspar, quartz, talc, and sodium silicate. The chemical composition of ceramic bonds is typically 65–70% SiO_2 , 20–25% Al_2O_3 , and approximately 10% of alkali and alkaline earth metal oxides. Figures 2.1 and 2.2 give some idea of the structure of an abrasive tool. They are photographs of polished sections prepared from regular alumina grinding wheels (grit 46, K-hardness and medium structure (6)). The general appearance of a section is shown in Fig. 2.1. The micrograph demonstrates the nonuniform structure of the grinding wheel. In places, the alumina grains are surrounded with a light film of the bond material, with fine bridges linking the grains and large open pores, while elsewhere the grains seem to be immersed in the bond, which contains fine closed pores.

Detailed examination of individual areas of the section clearly demonstrates that the nonuniformity is much greater than can be seen at low magnifications. Most of the section consists of grains or fragments of monocrystalline alumina (corundum). The grains are usually surrounded by fine rims of the bond material, which form bridges between the corundum grains. Adjoining bridges are separated by large round pores with smooth internal surfaces (Fig. 2.3). Aggregate grains, consisting of several corundum crystals cemented by slag interlayers, are broken down by the bond during firing, and individual corundum crystals become immersed in the glass, which frequently contains crystals produced by the interaction between the accessory minerals of alumina and the bond (Fig. 2.4).



Fig. 2.1 Abrasive tool body: dense alumina aggregates cemented with a vitreous bond. Reflected light, $\times 60$ magnification (Courtesy of Professor Givi Bockuchava)

Fig. 2.2 A meniscus of vitreous bond material between grains. Reflected light, $\times 250$ magnification (Courtesy of Professor Givi Bockuchava)

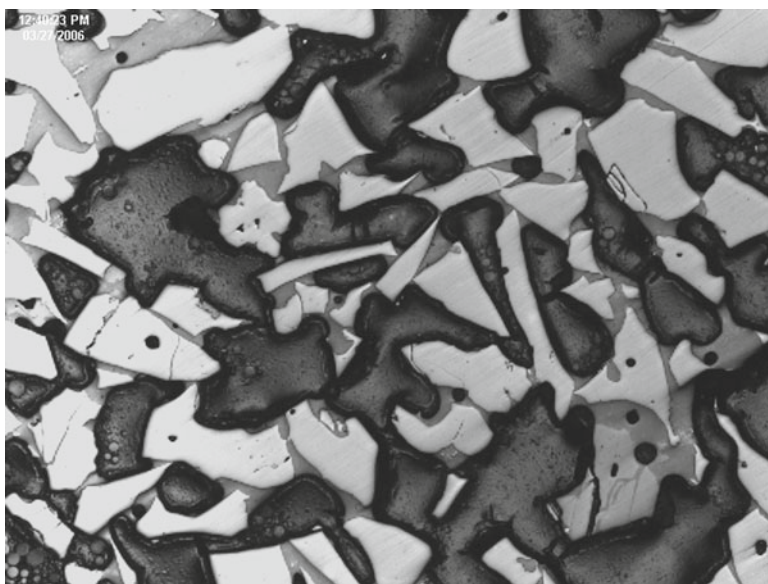


Fig. 2.3 A section of an abrasive tool showing adjoining bridges are separated by large round pores with smooth internal surfaces; an aggregate alumina grain broken down by the bond. The bond contains rutile aggregates (*white*), pores and microcracks (*black*). Reflected light, $\times 250$ magnification

Therefore, abrasive tools appear to be the most complex of silicate products, and it is quite evident that their properties, like those of any other silicate product, will be determined by their phase composition, the structure of the bond, the strength of its adhesion to the alumina grains.

Fig. 2.4 A section of an abrasive tool: an aggregate alumina grain broken down by the bond. The bond contains rutile aggregates (*white*), pores and microcracks (*black*). Reflected light, $\times 250$ magnification (Courtesy of Professor Givi Bockuchava)



2.2.1 Physicochemical Processes That Occur During Firing

Studies of ceramic bonds used in industry, both in their pure state and as part of alumina abrasive tools, have shown that the firing process converts bonds into nonuniform glass of complex composition, which on devitrification produces mullite, cordierite, spinel if the bond contains MgO, and anorthite and mullite if it contains CaO. The physicochemical processes occurring during the heat treatment of abrasive tools can be described as follows. Firing causes the bond to form a liquid phase, and as the temperature rises, this phase dissolves the other components of the bond, as well as the surface of alumina grains. The temperature at which the liquid phase first appears depends on the melting point of the most fusible component of the ceramic bond. In the industry, this is soluble glass (sodium silicate), which is either introduced into the bond in its solid state, or forms part of the solution used to wet the abrasive material during molding. Undoubtedly, if other oxides were also introduced into the bond in the form of more fusible compounds, they too would act as solvents and would react with the alumina.

However, because alumina is relatively soluble in alkali oxide components, the most active solvent is Na_2O . Since sodium silicate becomes quite mobile even at 650°C , it can be assumed that the dissolution of alumina (and of bond components) begins at this temperature. Initially, the concentration of Na_2O in the newly formed

Table 2.1 Fired chemical composition of several bonds and their firing resistance

Bond no	Chemical composition, wt%									Firing resistance (°C)
	SiO ₂	TiO ₂	Al ₂ O ₃	Fe ₂ O ₃	CaO	MgO	K ₂ O	Na ₂ O	Total	
1	67.68	1.34	16.58	2.40	1.45	0.54	Nil	9.91	99.88	1,150
2	67.73	0.80	12.50	1.70	1.40	0.60	–	14.80	99.53	970
3	67.48	Nil	3.04	1.27	1.40	0.82	–	25.74	99.75	650
4	69.14	1.14	11.31	1.91	5.40	0.62	–	10.14	99.66	1,060
5	67.92	1.20	11.56	1.94	1.25	5.10	–	10.66	99.63	1,090
6	67.72	0.45	13.02	2.36	0.40	0.56	5.43	10.08	100.02	1,080

Table 2.2 Determination of Al₂O₃ in these bonds, extracted from the samples after heat treatment at various temperatures

Bond no.	Al ₂ O ₃ content (%) of bonds heat treated at various firing temperatures (°C)						
	450	650	850	1,050	1,250	1,250 ^a	1,250 ^b
1	16.62	17.76	20.25	23.18	22.45	25.47	26.50
2	12.58	16.73	21.08	23.16	24.28	26.13	28.07
3	3.06	4.67	10.52	23.57	25.98	28.34	28.98
4	11.34	16.25	19.53	22.73	25.52	26.21	26.48
5	11.57	13.44	18.94	23.53	26.08	29.98	30.61
6	13.12	15.58	18.76	23.08	24.33	26.46	27.44

^aHolding at the final firing temperature (8 h)^bHolding at the final firing temperature (16 h)

liquid phase is relatively high, up to 25%. As the other bond components and alumina dissolve (as the temperature increases), the concentration of Na₂O in the melt falls, its viscosity rises, and at the holding temperature dissolution is virtually complete.

The interaction between alumina and the bond is illustrated by the figures contained in Tables 2.1 and 2.2. Table 2.1 gives the fired chemical composition of several bonds and their heat resistance, or temperature at which melting first occurs (also known as the bond softening temperature). Table 2.2 contains the results of determination of Al₂O₃ in these bonds, extracted from the samples after heat treatment at various temperatures. The tables demonstrate that there is a direct relationship between the amount of dissolved alumina, the final firing temperature, and the alkali content of the bond.

Irrespective of its initial value, the heat resistance reached by the bond material during the firing process is close to the abrasive tool holding temperature. This explains, why abrasive products can be fired at temperatures 200°C and even 300°C higher than the bond softening temperatures, without the bond leaking and the products being deformed. It is interesting to note that bond 5, which contains magnesium oxide and has high initial heat resistance, dissolved alumina faster than all the others. This is explained by the formation of spinel at the contact interface with alumina, which prevents rapid increase of the alumina content of the liquid phase and thus allows it to retain greater mobility.

As the material dissolves, new mullite, anorthite, cordierite, and spinel crystals appear in the liquid phase at 1,200°C. Thus, the first heating stage of the firing process is the phase of chemical reactions and physicochemical transformations through which the bond reaches a state of equilibrium and partial crystallization. During the holding period, the composition of the bond equalizes and new crystals appear. This is conditional on the local dissolution of alumina during the heating period causing its composition to move into the area of molten bond that is capable of devitrification. The holding period is therefore chiefly a period when new compounds formed in the bond crystallize out of the liquid phase.

During the cooling process, the viscosity of the bond increases so much that the crystallization of new compounds virtually ends. This is why the cooling pattern seems to play an important part, not in the sense of giving the bond a specific structure, but in the sense of preventing mechanical stresses arising in grinding wheels due to their heterogeneous composition, and, more importantly, due to the simultaneous presence of a crystalline component, i.e., alumina grains and the vitreous bond. The cooling period is essentially a period when physical changes take place in the grinding wheel. Studies have shown that the vitreous content of the bond determines the mechanical properties of the tool. The vitreous content of the bond increases from 75 to 100%, with resulting breaking strength increases from 100 to 200 kg/cm².

Of the minerals studied, the only one that appears to improve the mechanical properties of grinding wheels is spinel $\text{MgO} \cdot \text{Al}_2\text{O}_3$, which is formed at the contact of the bond with alumina and encloses its grains in a casing of fine octahedra, no larger than 8 μm in diameter. The Na_2O contained in the tool dissolves the alumina grain, forming a small area of melt enriched with Al_2O_3 , thus aiding the formation of spinel. The dissolution of up to 4% of alumina in the bond increases the mechanical strength of the grinding wheel, provided that the bond retains its vitreous structure, or small quantities of minerals form at the contact interface.

Ceramic bond materials producing abrasive tools with good mechanical properties are those located near the SiO_2 apices of the tetrahedra of two systems: $\text{Na}_2\text{O}-\text{K}_2\text{O}-\text{Al}_2\text{O}_3-\text{SiO}_2$ and $\text{Na}_2\text{O}-\text{MgO}-\text{Al}_2\text{O}_3-\text{SiO}_2$, containing these materials in the following proportions: $\text{SiO}_2=70-75\%$; $(\text{K}_2\text{O})\text{MgO}=5\%$; $\text{Al}_2\text{O}_3=15-10\%$, and $\text{Na}_2\text{O}=10\%$. In modern grinding wheel firing conditions, these compounds react vigorously with alumina. In this process, the bond is enriched with Al_2O_3 , whose content (in the four-part system) rises to 30–35%. These compounds form glass that does not devitrify during firing and produces grinding wheels with breaking strengths of 170–200 kg/cm².

2.2.2 Ceramic Bond Minerals That Form During Firing

Alongside anorthite, mullite, cordierite ($2\text{MgO} \cdot 2\text{Al}_2\text{O}_3 - 5\text{SiO}_2$), and spinel, which form in the bond when it is enriched with alumina, firing gives rise to other new formations, produced by the interaction between the bond and the accessory minerals

Fig. 2.5 A bond interlayer separating alumina grains and consisting of plagioclase (gray) with anatase interpenetrations (white). Reflected light, $\times 300$ magnification (Courtesy of Professor Givi Bockuchava)

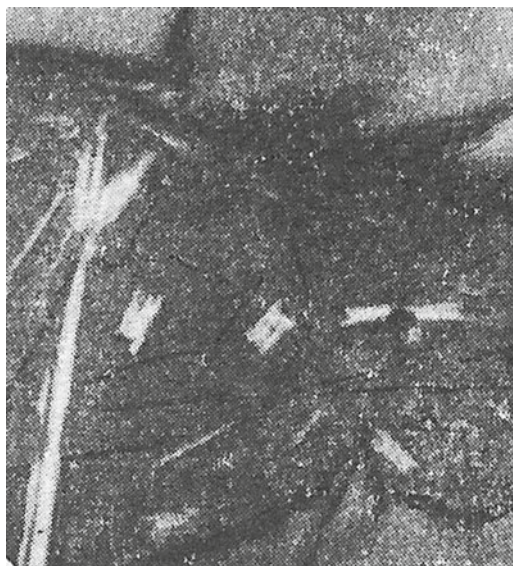
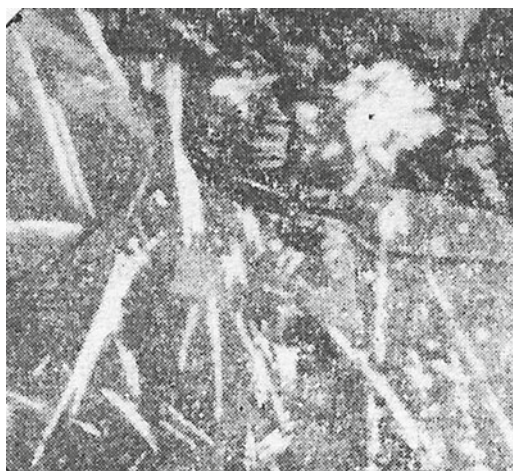


Fig. 2.6 Mullite (pale gray), anatase (white elongated sections), magnetite (white dendrites), and rutile (round white formations) in glass separating fractured alumina grains. Reflected light, $\times 250$ magnification (Courtesy of Professor Givi Bockuchava)



present in alumina. They include plagioclases, anatase, hematite, magnetite, and rutile. Let us now consider the process of formation of each of these minerals.

Anorthite glass (slag) contained in regular alumina grains in the form of streaks or interlayers is dissolved by the bond. The composition of the bond is significantly changed as a result, and on crystallization it forms plagioclase and anatase (Fig. 2.5). Silica-rich slag is also absorbed by the bond, but does not disturb its vitreous structure. The resultant sections of the grinding wheel usually consist of glass containing small quantities of mullite prisms, acicular rutile crystals, and magnetite dendrites (Fig. 2.6).

Fig. 2.7 A portion of the bond between alumina grains: the formation of granular rutile aggregates (*white*) through the oxidation of titanium carbide (*white*) embedded in the alumina. The bond contains large pores (*white*). Reflected light, $\times 250$ magnification (Courtesy of Professor Givi Bockuchava)



Titanium oxides occurring in glass present as accessory minerals in alumina convert into disperse rutile grains on firing. The grains are then recrystallized in the bond, forming acicular aggregates. Anosovite behaves differently, converting into a pseudo-morph after anatase and appearing in the bond in the form of brown colored crystals. Titanium carbide and nitride oxidize during firing forming granular rutile aggregates. Polished sections distinctly show the explosive nature of their oxidation and its adverse effects—presence of crystallization of the rutile in the bond and the formation of gas bubbles (Fig. 2.7). In addition, during the firing process, the action of Na_2O present in the bond causes the solid solution of Ti_2O_3 in alumina to break down and a fringe of rutile needles form on the surfaces of the alumina crystals (Fig. 2.8).

Measurements have shown that the solid solution of Ti_2O_3 in alumina crystals break down to a depth of 30–40 μm . The presence of ferroalloy has a dramatic effect on bond composition. The bond material surrounding the ferroalloy bead is saturated with hematite and magnetite formed through ferroalloy oxidation (Fig. 2.9). Titanium sulfide and carbide present in industrial monocrystalline alumina grains also convert to rutile during firing, forming granular aggregates distributed in the bond. A grinding wheel bond usually contains up to 20–25% of neocrystalline formations, with crystal sizes not exceeding 40–50 μm . If the bond is overfired, these crystals reach 80–120 μm and develop microcracks in the bond (Fig. 2.10). The features of minerals formed in grinding wheels after firing, which form the basis of microscopic analysis, are described below.

Anorthite ($\text{CaO} \cdot \text{Al}_2\text{O}_3 \cdot 2\text{SiO}_2$) appears in the bond in the form of randomly arranged colorless lamellae and columnar (elongated tabular) crystals displaying negative elongation and polysynthetic twinning. Moderate refractive index and birefringence: $N_g = 1.588 \pm 0.002$, $N_p = 1.575 \pm 0.003$, $N_g - N_p = 0.013$.



Fig. 2.8 A fringe of rutile needles at the alumina-bond contact. Reflected light, $\times 250$ magnification (Courtesy of Professor Givi Bockuchava)

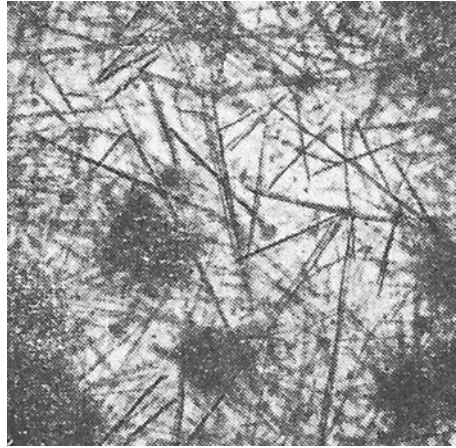
Fig. 2.9 Ferroalloy and iron oxides in bond material. Reflected light, $\times 250$ magnification (Courtesy of Professor Givi Bockuchava)



Fig. 2.10 An anorthite spherulite in bond material showing microcrack formation. Analyzer out, $\times 200$ magnification (Courtesy of Professor Givi Bockuchava)



Fig. 2.11 Mullite in bond material. Analyzer out, $\times 80$ magnification (Courtesy of Professor Givi Bockuchava)



Mullite ($3\text{Al}_2\text{O}_3 \cdot 2\text{SiO}_2$) is always colorless in the bond (Fig. 2.11). It crystallizes in the form of fine needles, mostly gathered into felted and radiated aggregates. Moderate refractive index and birefringence: $N_g = 1.654 \pm 0.002$, $N_p = 1.642 \pm 0.003$, $N_g - N_p = 0.012$.

Cordierite ($2\text{MgO} \cdot 2\text{Al}_2\text{O}_3 \cdot 5\text{SiO}_2$ (Fig. 2.12)) crystallizes in the form of colorless short prismatic pseudo-hexagonal crystals (in the rhombic system), which have a



Fig. 2.12 Cordierite in bond material. Analyzer out, $\times 160$ magnification (Courtesy of Professor Givi Bockuchava)

moderate refractive index and low birefringence: $N_g = 1.525 \pm 0.003$, $N_p = 1.521 \pm 0.002$, $N_g - N_p = 0.004$. In polished sections, it is dark gray, with low reflectivity and a relief similar to that of glass.

Spinel ($\text{MgO} \cdot \text{Al}_2\text{O}_3$) is yellow or colorless in transmitted light (Fig. 2.13). It appears in the form of octahedra and grains at the alumina contact. It has a high refractive index: $N = 1.722 \pm 0.003$.

Plagioclases crystallize in the triclinic system. In transmitted light, they appear in the form of elongated tabular crystals, frequently displaying polysynthetic twinning. Moderate refractive index and birefringence: $N_g = 1.553 - 1.558$, $N_p = 1.547 - 1.552$. In polished sections they are gray, with low reflectivity and relief equal to that of as glass.

Hematite (Fe_2O_3) crystallizes in the trigonal system. In transmitted light, it appears in the form of orange-red irregular accumulations, less often in the form of hexagonal or triangular lamellae. High refractive index and birefringence: $N_g = 3.01$ Li, $N_p = 2.78$ Li. The irregular accumulations result from ferroalloy oxidation, while the regular lamellae, frequently with regular orientation, appear on the surfaces of alumina crystals (Fig. 2.14). They are formed by the recrystallization of ferrous oxide film on alumina grains (in monocrystalline alumina). In reflected light, hematite is white, with above-average reflectivity and a higher relief than glass.

Magnetite (Fe_3O_4) crystallizes in the cubic system. It is opaque. In transmitted light it appears in the form of irregular black accumulations associated with ferroalloy, less often in the form of fine cubic crystals and skeletal cruciform dendrites. In reflected light, it is white with high reflectivity and a higher relief than glass.

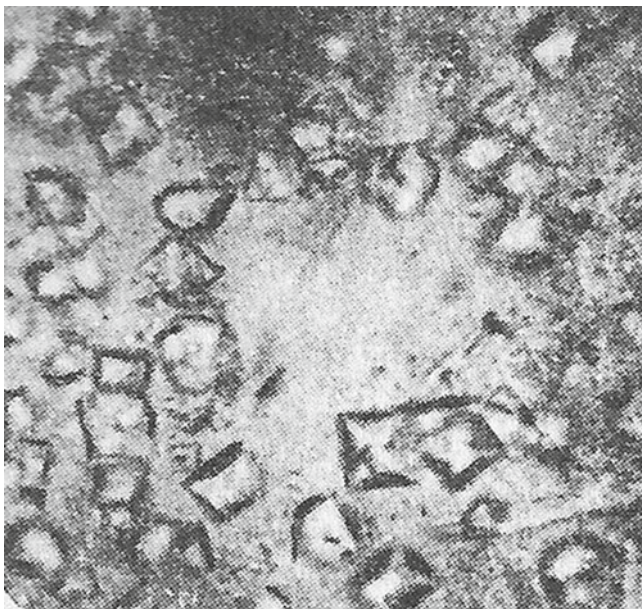


Fig. 2.13 Spinel in bond material. Analyzer out, $\times 250$ magnification (Courtesy of Professor Givi Bockuchava)

Fig. 2.14 Hematite on the alumina-bond contact. Reflected light, $\times 150$ magnification (Courtesy of Professor Givi Bockuchava)



Rutile (TiO_2) crystallizes in the tetragonal system. It is colorless, and forms either granular formations or acicular or prismatic (frequently hollow) crystals. Its refractive index and birefringence are extremely high: $N_g = 2.903$, $N_p = 2.616$. In reflected light, it appears as either sinuous lacy aggregates and accretions formed by the oxidation of titanium carbide and nitride, or in the form of white rectangular and rhomboid sections, formed by the alteration of anosovite. It has high reflectivity and a relief higher than glass.

Anatase (TiO_2) crystallizes in the tetragonal system, forming prismatic and rod-like crystals, which can be either colorless or colored yellow or brown. Its refractive index and birefringence are very high, $N_g = 2.56 \pm 0.02$, $N_p = 2.48 \pm 0.02$. In reflected light, it appears in the form of white, rectangular, and rhomboid sections. It has above-average reflectivity and a relief higher than glass.

The following case studies highlight the importance of interface compounds and bonding phases on grinding wheel wear in high-performance vitrified grinding wheels. It should be noted that these studies are focused on clay-based bonding systems.

2.3 Case Study I: Interfacial Compounds and Their Effect on Grinding Wheel Wear

The type of grinding wheel considered in this case study is made using aluminum oxide ($\alpha\text{-Al}_2\text{O}_3$), a hard material with a Knoop hardness of up to $2,000 \text{ kg/mm}^2$, is used in the grinding industry in two principal forms: a high purity, fused form of alumina containing over 99.9 wt% Al_2O_3 that is white in appearance; and a fused, brown colored, alumina of 95 wt% purity. The main impurity in this latter form is TiO_2 at a level no greater than 3 wt%. This tends to increase the toughness of the grain and is accompanied by other impurities such as MgO , CaO , Fe_2O_3 , and ZrO_2 . Other grinding wheels described in this case study use cubic boron nitride (CBN) that has a Knoop hardness in excess of $4,500 \text{ kg/mm}^2$.

The range of vitreous bonding systems and abrasive types is very large, though only aluminosilicate and aluminoborosilicate bonding systems are used by the abrasive wheel industry. The normal practice is to adjust the proportions of Al_2O_3 , B_2O_3 , SiO_2 , and alkali oxides to achieve the desired fluidity. Other chemical and physical properties can be modified by the addition of alkaline earth oxides. Vitreous bonds are composed of mixtures of quartz, feldspar, clay, borate minerals, and ground frits. In practice, the bonds are mixed with a variety of abrasive grains. However, this case study considers high purity and titanium-doped varieties (using a typical mesh size of 220, which is approximately $62 \mu\text{m}$ diameter abrasive grain size) and CBN with B64 grain size (approximately $63 \mu\text{m}$ in diameter).

The grinding process is accompanied by wear of the abrasive wheel, and the rate of this wear plays an important role in determining the efficiency of the grinding process and the quality of the workpiece. The structure of a vitrified grinding wheel

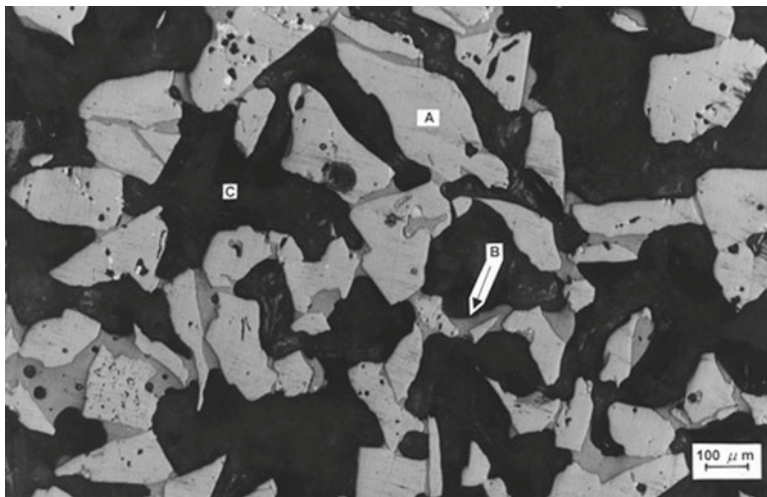


Fig. 2.15 Microstructure of a vitrified grinding wheel. A—denotes abrasive grain, B—denotes vitrified bonding phase, and C—represents distributed porosity

is composed of abrasive grains, a bonding system, and a large number of pores. Figure 2.15 shows a typical porous grinding wheel structure [70]. Krabacher [71] pointed out that wear mechanisms in grinding wheels appear to be similar to that of single-point cutting tools, the only difference being the size of swarf particles generated. The wear behavior observed is similar to that found in other wear processes; high initial wear followed by steady-state wear. A third accelerating wear regime usually indicates catastrophic wear of the grinding wheel, which usually means that the wheel will need to be dressed. This type of wear is usually accompanied by thermal damage to the surface of the ground workpiece. The performance index used to characterize wheel wear resistance is the grinding ratio, or G-ratio, and is expressed as the ratio of the change in volume of the workpiece ground to the change in the volume of the grinding wheel removed, thus,

$$G = \frac{\Delta v_w}{\Delta v_s} \quad (2.1)$$

Grinding ratios cover a wide range of values ranging from less than 1 mm³/mm³ for vanadium-rich high-speed steels to over 60,000 mm³/mm³ when internally grinding bearing races using CBN abrasive wheels. Attempts have been made on how to address the problems related to the wear of abrasive grains in terms of the theory of brittle fracture. The conclusions of various researchers lead us to believe that the variety of different and interacting wear mechanisms involved, namely, plastic flow of abrasive, crumbling of the abrasive, chemical wear, etc., makes grinding wheel

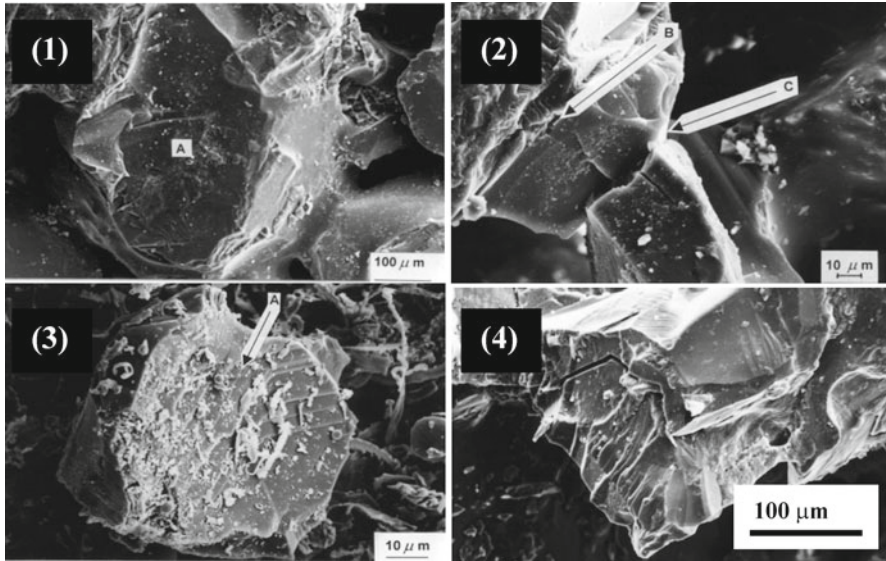


Fig. 2.16 Grinding wheel wear mechanisms: (1) abrasive wear—A denotes a wear flat generated by abrasion; (2) bond bridge fracture—A denotes the abrasive grain, B denotes the interfacial bond layer, and C denotes a crack passing through the bond bridge; (3) abrasive grain fracture—A denotes crystallographic grain fracture; and (4) interface fracture between abrasive grain and bond bridge

wear too complicated to be explained using a single theoretical model. High efficiency precision grinding processes place extreme loads onto the grain and the vitrified bonding bridges.

2.3.1 Wear Mechanisms

Four distinct wheel wear mechanisms that contribute to the wear of grinding wheels are identified as (Fig. 2.16):

1. Abrasive wear (formation of wear flats on the surface of abrasive grains)
2. Fracture of bond bridges
3. Fracture of abrasive grains due to mechanical and thermal shock loads
4. Fracture at the interface between abrasive grain and bond bridge

2.3.1.1 Abrasive Wear

The formation of wear flats on abrasive grains leads to a loss of grain sharpness. The sources of minute scale wear are:

1. Wear due to frictional interaction between workpiece and abrasive grain
2. Plastic flow of the abrasive grain at high temperature and pressure
3. Crumbling of the abrasive grain due to thermal diffusion and microscale mechanical impact
4. Chemical reaction between abrasive and workpiece material at elevated temperatures and in the presence of grinding fluids

The latter mechanism can reduce the resistance of the abrasive grain to other wear mechanisms. Dull abrasive grains are caused by the generation of wear flats on active grains that leads to an increase in the area of contact and frictional interactions between abrasive grain and the workpiece. At the point of dulling of the abrasive grain, very high temperatures exist in the area of contact that greatly enhances adhesion and chemical reaction between two surfaces. If grain and bond bridge fracture does not occur during grinding then the plateau area on the grain widens and the rate of wear increases. If fracture is delayed further, as with hard grinding wheels, then the wheel becomes glazed and the workpiece is thermally damaged.

It has been shown experimentally [72] that chemical affinity between the abrasive and the workpiece material can be used as a guide for the selection of grinding wheels. Their observations of solid diffusion of silicon carbide into ferrous materials explain the catastrophic wear rates exhibited by these “wheel–workpiece” combinations. The most common method used for measuring wear flat area employs an optical or an electron microscope. Hahn [73] observed and analyzed the effect of the increasing wear flat area during the plunge grinding of various workpiece materials. Hahn concluded that grinding forces gradually increase during wear-flat formation up to a point where the grinding wheel will restore its sharpness due to abrasive grain fracture.

2.3.1.2 Fracture Wear

The occurrence of abrasive grain and bond fracture are considered simultaneously for the following reasons:

1. They are of the same nature, i.e., fracture of brittle materials and hence the theory of brittle fracture is applicable to both bonding bridge and abrasive grain. The applied thermal and mechanical loads, usually under cyclic conditions, cause initiation and further development of cracks that leads to fracture and the formation of new irregular surfaces.
2. They are related to dressing methods used and occur simultaneously. The initial and final stages of wheel life between dressings exhibit fracture wear that is a combination of abrasive grain and bonding bridge fracture.
3. The relative amounts of bond bridge and abrasive grain wear cannot always be calculated. An investigation into precision grinding employed a soft wheel that gave a high percentage of bond fracture, whereas a harder wheel gave partial abrasive grain fracture. Wear by attrition occurred in both cases.

However, the combination of grinding parameters such as equivalent chip thickness and the grindability of the workpiece material determines the effective wheel

hardness, and so no single feature of the grinding process can be used to predict the fracture pattern of the wheel in advance. The difficulty when relating grinding wheel wear due to fracture to a particular grinding condition arises from the lack of knowledge about the loads applied to both abrasive grains and their bonding bridges and their response to these applied loads.

Tarasov [74] suggests that abrasive grain fracture occurs as a result of mechanical forces due to chip formation, or thermal shock, induced by instantaneously high temperatures. Hahn [73] proposed a thermal stress hypothesis to explain the fracture of abrasive grains. Plunge grinding experiments were conducted under fixed normal load conditions. Hahn asserted that as wear progresses measurements of torque indicated that the tangential force decreases. This led to the conclusion that abrasive grain fracture due to mechanical loading will not occur. Mechanical stresses wear also considered as an explanation for the different rates of wear of the grinding wheels used in the experiments.

Bhattacharyya et al. [75] observed abrasive grain loss due to fracture using an electron microscope. They concluded that they could not differentiate between Peklenik's crystal splintering, i.e., grit flaking due to thermal stress, and abrasive grain fragmentation. However, they did explain their results in terms of Hahn's thermal shock hypothesis. Hahn's experimental conditions suggested that attrition of the abrasive was expected to occur through abrasive wear. Wear measurements by Hahn [73] were based on the reduction in grinding wheel diameter, which Malkin and Cook [76] attributed to abrasive wear. Wear rates recorded were of the order of 50 $\mu\text{in./s}$. It was expected that abrasive wear rates were in the region of 5 $\mu\text{in./s}$. This rate was observed under light grinding conditions. Under heavy grinding conditions, the conditions of wear appeared to be more complex.

Malkin and Cook [76] collected wheel wear particles for each grade of grinding wheel when grinding using a fixed set of operating conditions. They analyzed their size distributions statistically and discovered that a soft-grade grinding wheel (G-grade) produces 85% of grinding debris associated with bonding bridge fracture, whilst a harder-grade grinding wheel (K-grade) produces 55% of grinding debris associated with fractures of bonding bridges. Abrasive wear accounted for 4% of the total wear in both cases.

The strongest evidence in support of the idea of fracture due to mechanical loading is that fracture occurs some distance away from the cutting edge [77]. It was concluded that the heat generated by cutting has no effect on abrasive grain fracture since the peak temperature of the abrasive grain occurs at the surface of the grain in contact with the workpiece where fracture is initiated on cooling according to the thermal stress hypothesis. The hypothesis does not take account of any difference in the coefficient of thermal expansion between abrasive grain and bond bridges, and also the effect of thermal shocks on the quenching action of grinding fluids on the abrasive grain leaving the cutting zone. The latter case was analyzed and it was reported that the thermal stress in an abrasive grain due to a pulsating heat source showed that the magnitude of the maximum tensile stress is not large enough to cause fracture of the grain. Malkin and Cook [76] adopted the mechanical loading

approach. Malkin and Cook [76] derived an expression from first principles for the probability of bond fracture in terms of a bond stress factor.

Although bond and grain fracture are similar mechanisms, they have a different effect on the economics of the grinding process. The first mechanism results in a rapid loss of the grinding wheel, while the second mechanism, on a comparable scale with the un-cut chip thickness, generates sharp cutting edges and is known as the “self-dressing action.” Both mechanical and thermal stresses appear to be responsible for fracture wear. The effect of heat at the abrasive grain and workpiece interface is responsible for locally affecting the mechanical properties of the abrasive grain. However, fragments of larger sizes of abrasive grain are more likely to occur through mechanical loading that governs bond fracture and the self-sharpening action. A method of alleviating the onset of bond fracture due to unusually large mechanical loads is to dissolve deleterious particles in the bonding system that weakens the structure of the bonding bridge.

In vitrified bonds, these particles are quartz particles that naturally occur in ceramic raw materials. These particles reduce the load-bearing strength of the bonding bridges during vitrification heat treatment. The study of the effect of the elastic modulus on the fracture behavior of vitrified abrasive grinding wheels was conducted by Decneut, Snoeys, and Peters [9]. They discovered that vitrified grinding wheels with a high modulus of elasticity wear by a mechanism of abrasive grain fracture rather than fracture of the glass bond bridges that hold the abrasive grains in place. As the modulus of elasticity increases the “self-sharpening effect” is lost because abrasive grains cannot be released from the bonding matrix. This leads to a condition where the temperature of the workpiece material begins to increase and is associated with phase transformations and thermal cracking of the surface layers that results in a reduction in fatigue strength.

In this case, the performance of the abrasive grinding wheel for a specific metal removal rate and workpiece material depends on the selection of the appropriate grade of abrasive grinding wheel that is a function of its modulus of elasticity and strength. In the present study, the elastic modulus, bending strength, and nature of fracture was found to be dependent on the vitrification behavior of the glass bonding system, the amount of bond, and the type of abrasive grain used in the vitrified grinding wheel. It was found that the wear of vitrified grinding wheels is highly dependent on the way the grinding wheel “vitrifies” during heat treatment.

2.3.2 Microstructure of Abrasive Grains

2.3.2.1 High Purity Aluminum Oxide

Examination of high purity aluminum oxide in a scanning electron microscope using an electron probe microanalyzer showed that 99.5 wt% of the grain was Al_2O_3 with the balance consisting of Na_2O and SiO_2 in equal proportions.

However, local Na_2O -enriched areas were observed within parts of the grain. Figure 2.17 shows the areas of Na_2O local enrichments within the grain as white

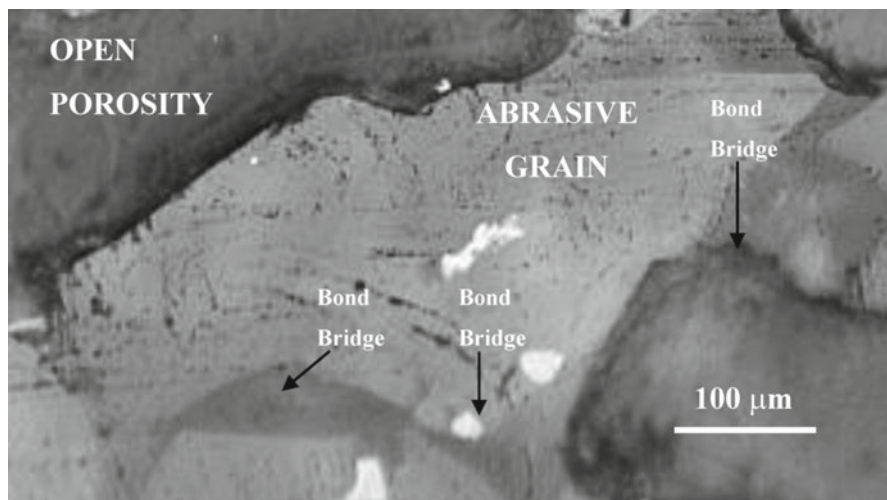


Fig. 2.17 High purity aluminum oxide grinding wheel showing enriched regions of Na₂O (denoted by black arrows) determined using an electron probe microanalyzer

reflections when viewed under an optical microscope. Under close examination, high purity aluminum oxide contains aluminum oxide, sodium aluminate, carnegieite, sodium monoaluminate, nepheline, and glass of variable composition. In heat-treated high purity abrasive grains, preferential etching at the surface of the grain appears to occur along crystallographically controlled directions (Fig. 2.18). This is assumed to be due to the dissolution of planar blocks of β -Al₂O₃ (Na₂O·11Al₂O₃) that is present in the α -Al₂O₃ host material. X-ray diffraction of high purity alumina established the existence of β -Al₂O₃ prior to the optical examination of the abrasive grains. Other impurities found include rarely seen calcium-rich platelets in the form of alite (Ca₃SiO₅), and an unnamed oxide, NaCaAlO₃, which is known to have several polymorphic forms.

2.3.2.2 Titanium-Doped Aluminum Oxide

The amount of TiO₂ in titanium-doped aluminum oxide was measured using an electron probe and was found to be in the range of 1–2 wt%. The amount of titania present is inconsistent with earlier work that had determined that the maximum solubility of TiO₂ in Al₂O₃ is less than 0.3 mol% at 1,300°C [79]. Although some of the excess can be accounted for in the formation of Ti₂O₃, it is possible that not all titania is in solid solution. This was confirmed by the occurrence of blade-like inclusions that is consistent with rutile (TiO₂) needle morphology. This would account for the variability in measured titania and its presence in amounts greater than its solubility in Al₂O₃. In heat-treated and titanium-doped aluminum oxide, calcium

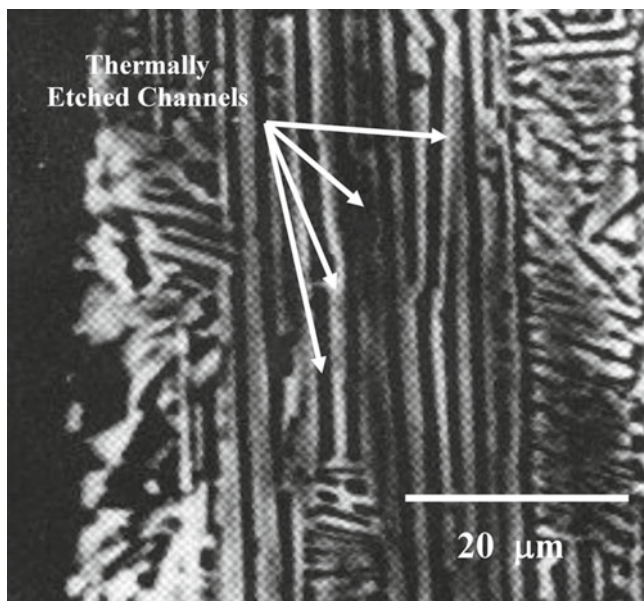


Fig. 2.18 High purity aluminum oxide grain showing thermally etched channels of $\beta\text{-Al}_2\text{O}_3$ layers that are present in the $\alpha\text{-Al}_2\text{O}_3$ structure

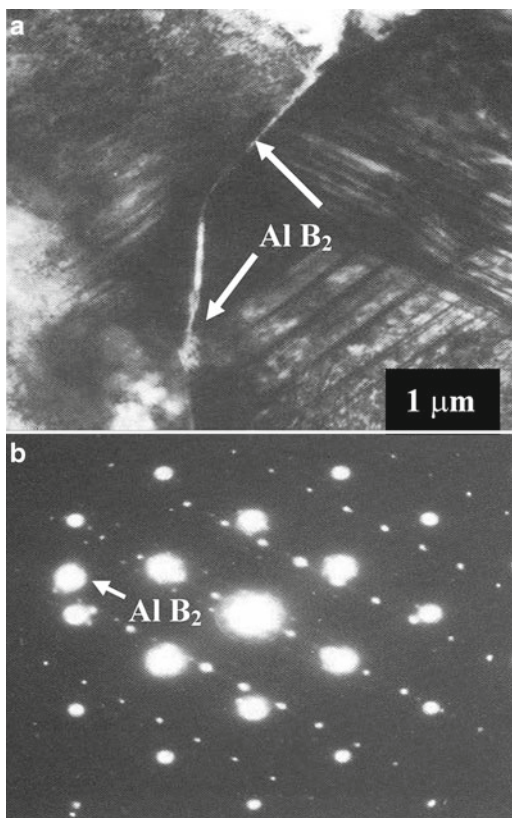
hexaluminate, anorthite, and spinel are not affected by the heat treatment process. However, glass is devitrified forming anorthite spores. Titanium minerals are oxidized to higher oxides such as anatase and rutile. These changes are accompanied by large changes in volume that may affect the performance of any abrasive tool. As a precaution, Ti-doped aluminum oxide must be heated to $1,000^\circ\text{C}$ before it can be used for making abrasive cutting tools.

2.3.2.3 Cubic Boron Nitride

Cubic boron nitride (CBN) abrasive grains are made by compacting grains of CBN in the presence of aluminum. Aluminum reacts with BN to form a mixture of AlN and AlB_2 that forms a stable and catalytically inactive binder. Interaction between aluminum and BN is intimate and can be observed directly using scanning and transmission electron microscopes. There is very little interaction between CBN grains. The edges of CBN grains not in contact with each other form rinds of AlN in thin, continuous lines with several nodules along its length.

The rind that encloses the exposed CBN grain is always orientated so that it has crystallographic directions parallel to particular directions in the CBN lattice. The selected area diffraction pattern shown in Fig. 2.19 shows a $[110]$ CBN pattern with a rectangular AlN $[11\bar{2}0]$ pattern superimposed. The AlN has grown with its basal

Fig. 2.19 (a) Two contacting CBN grains separated at intervals by an AlN rind which is parallel to the CBN [110] planes. The outer edges of the grains are in contact with a featureless AlB₂ layer. (b) Selected area diffraction pattern from part of the field of contact showing the relative orientation of phases present. The *smaller spots* are AlN, and the *larger spots* are CBN. The *arrow* indicates the single spot generated by AlB₂ phase



planes parallel to the CBN facet plane. This orientation with CBN (110)//AlN (0001) and CBN [110]//AlN [11 $\bar{2}$ 0] is the most common orientation observed even when facet planes deviate away from being octahedral. At cube surfaces the orientation CBN (001)//AlN (0001) and CBN [110]//AlN [11 $\bar{2}$ 0] occurs. While most of the AlN can be located at CBN grain surfaces, AlB₂ nucleates independently in liquid aluminum at the later stages of consolidation. A single crystal of AlB₂ produces the reflection to the left of the SAED pattern that produces a single bright spot [80].

2.3.3 Experimental Procedure

2.3.3.1 Measurement of Mechanical Properties

The experimental procedure involved making experimental samples of abrasive grain and glass bond as a vitrified product using high purity aluminum oxide, titanium-doped aluminum oxide, and CBN bonded with an alumino-borosilicate bond

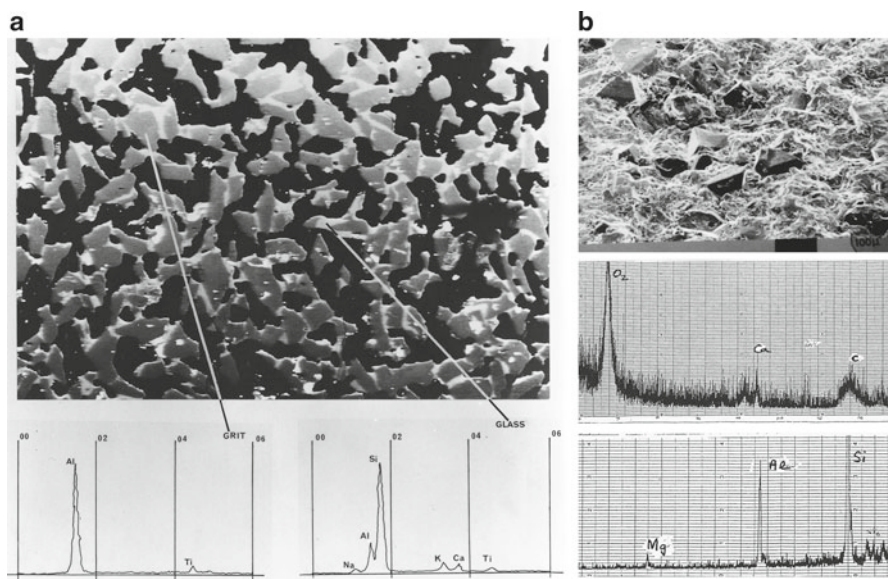


Fig. 2.20 Electron probe microanalysis of (a) titanium-doped aluminum oxide and vitrified glass bonding system, and (b) CBN and vitrified glass bonding system

containing 61.4 wt% SiO_2 , 17 wt% Al_2O_3 , 0.4 wt% Fe_2O_3 , 3.2 wt% CaO , 0.1 wt% MgO , 2.7 wt% Na_2O , 3.1 wt% K_2O , and 10.1 wt% B_2O_3 . Experimental samples were made by pressing abrasive grains and glass bond ingredients to a known density. The samples were moulded in the form of bars. The dimensions of the bars were 60 mm length, 12 mm height, and 12 mm depth. The samples were fired at the vitrification temperature (between 1,000 and 1,300°C) for 6 h in an electric furnace. The samples were prepared for four-point loading and for measuring their elastic modulus using the sonic method developed by [78]. A total of 20 experimental test samples were loaded in uniaxial tension. The Weibull modulus for the fractured samples was calculated to be 18.3 for aluminum oxide samples and 18.8 for CBN samples. A section of one of the bar samples was cut, mounted in resin, and polished to reveal the nature of bonding between glass and aluminum oxide. Figure 2.20 shows the section revealing abrasive grains bonded together by the vitrified glass bonding system. The black areas represent the pores between abrasive grains that are essential to provide free space for chips of metal and for coolant access. Figure 2.20 also shows the characteristic X-ray spectra for abrasive grains and glass bond. The abrasive grain spectrum shows aluminum and titanium (indicative of titanium-doped aluminum oxide), and the glass bond spectrum shows elements such as potassium, calcium, and sodium that are glass network-modifying elements, and aluminum and silicon that are network-forming elements. For the vitrified CBN grinding wheel, the bonding system contains magnesium, aluminum, silicon, calcium, and oxygen.

2.3.3.2 Manufacture of Grinding Wheels

Grinding wheel segments were made by pressing abrasive grains and glass bond ingredients to a known density. The samples were moulded in the form of segments to be attached to a pre-balanced grinding wheel body. The dimensions of the segments were 60 mm length, 15 mm height, and 20 mm depth. The samples were fired at the vitrification temperature (between 1,000 and 1,300°C) for 6 h in an electric furnace. Once fired, the segments were measured in terms of their hardness and grade and were bonded onto a steel backing using a high strength adhesive. The steel backings were then bolted onto a steel body containing the rest of the abrasive segments.

2.3.3.3 Measurement of Wear

The method of grinding wheel wear measurement adopted was the “razor blade” technique. The method involves grinding a workpiece that is less wide than the grinding wheel. A groove is worn into the wheel profile, which was measured with reference to the non-grinding portion of the grinding wheel using a razor blade. The grinding wheel was initially dressed using a single-point diamond and the wheel conditioned until steady-state grinding wheel wear was achieved. In order to achieve the conditions of bond fracture, the depth of cut for all experiments was set at 10 μm per pass with a table speed of 0.2 m/s and a grinding wheel speed of 60 m/s.

Immediately after the grinding experiments were performed, the razor blade was then lowered into the grinding position with the grinding wheel touching the blade. After grinding the blade, the wear of the grinding wheel was measured using a surface profilometer. The grinding ratio was calculated by measuring the volume of the grinding wheel removed and the volume of the workpiece removed.

2.3.4 Experimental Results

2.3.4.1 Mechanical Properties

The relationship between the elastic modulus and firing temperature as a function of abrasive grain type and bonding content is shown in Fig. 2.21 for both high purity and titanium-doped aluminum oxide structures. It is shown that the elastic modulus is developed as the vitrification temperature is increased and is highly dependent on the amount of bonding material that surrounds the abrasive grain. This is confirmed in Fig. 2.22, which shows the effect of the increase in bonding content on the elastic modulus at three different vitrification temperatures for high purity aluminum oxide structures. An interesting observation is that up to the softening point of the glass bond, high purity and titanium-doped aluminum oxide vitrified structures developed strength in the same way then declines for titanium-doped aluminum oxide structures depending on the amount of bonding material. The relationship is shown in Fig. 2.23. The same general trends are observed with vitrified CBN grinding wheels.

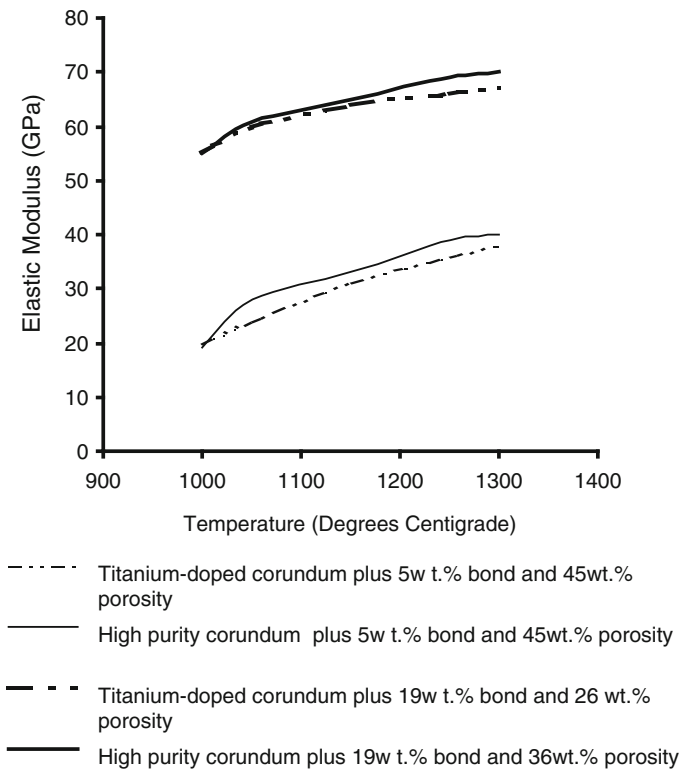
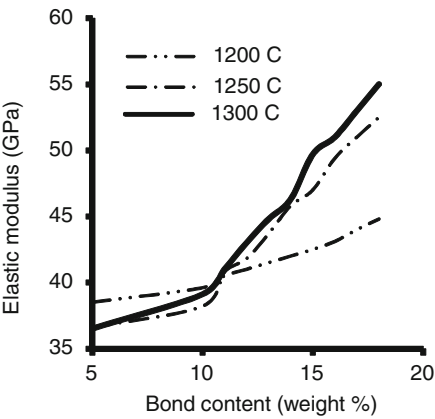


Fig. 2.21 Elastic modulus as a function of firing temperature for a number of abrasive grain types and bond contents

Fig. 2.22 Effect of bond content and firing temperature on the elastic modulus of high purity aluminum oxide structures



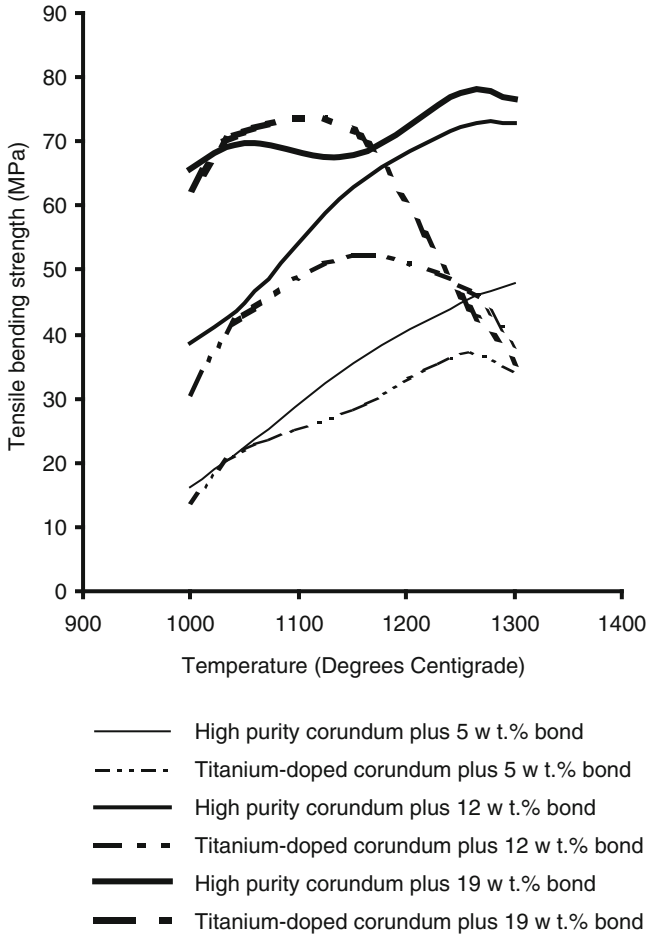


Fig. 2.23 Relationship between bending strength and firing temperature as a function of abrasive grain type and bond content

2.3.4.2 Wear of Grinding Wheels

The relationship between the wheel wear parameter, grinding ratio (G), and the firing temperature is shown in Fig. 2.24 for both high purity and titanium-doped aluminum oxide grinding wheel structures containing a different amount of vitrified bonding material. Again, the observation that up to the softening point of the glass bond, high purity and titanium-doped aluminum oxide structures develop wear resistance in the same way is noteworthy. Figure 2.24 shows that the grinding ratio is a function of vitrification temperature, but at a certain temperature, it is highly dependent on the type of abrasive grain used in the grinding wheel and the amount of bonding material used.

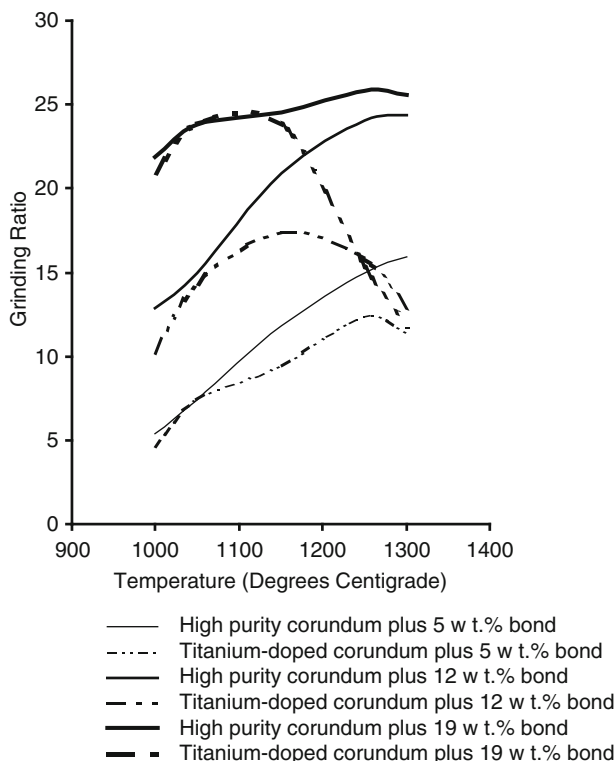


Fig. 2.24 Relationship between grinding ratio and firing temperature as a function of abrasive grain type and bond content

Examination in a scanning electron microscope showed that certain parts of the glass bond had devitrified in both high purity and titanium-doped aluminum oxide structures. The crystals are elongated with square sections and have a high Al_2O_3 content. An X-ray diffraction spectrum indicated that the phase is an aluminoborate solid solution. The best match was with $\text{Al}_{18}\text{B}_4\text{O}_{33}$. In addition to this phase, a second crystalline phase was observed in titanium-doped aluminum oxide structures. The phase consists of needles of rutile (TiO_2) orientated on the faces of titanium-doped aluminum oxide grains that penetrate into the glass bond. Figure 2.25a, b shows orientated rutile needle formation in the glass bond emanating from the aluminum oxide crystals. The structure in Fig. 2.25b was etched with a solution of 40% hydrofluoric acid in water. Figure 2.25c shows the growth of rutile needles from the interface between aluminum oxide and the glass bond using the electron backscatter mode. Figure 2.25d shows the devitrification of glass in the form of $\text{Al}_{18}\text{B}_4\text{O}_{33}$ crystals.

Fractured samples revealed a higher proportion of intergranular fracture than cut and polished samples. High purity aluminum oxide did not exhibit intergranular fracture at the interface between abrasive and bond but did exhibit the bond fracture mode. It appears that titania is an undesirable constituent in bonding systems that

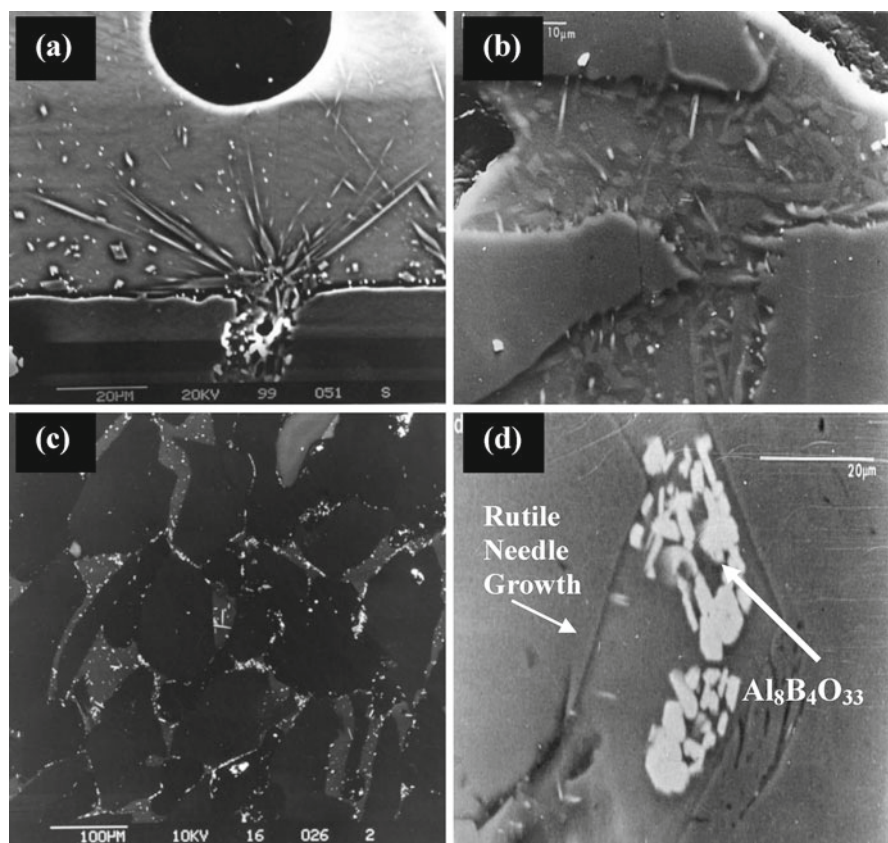
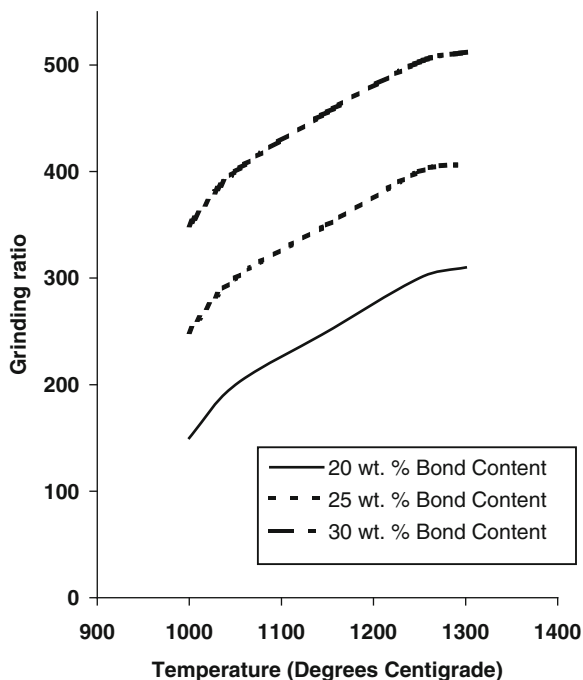


Fig. 2.25 (a) Titania (TiO_2), in the form of rutile needles, on the surface of the vitrified glass bond; (b) vitrified glass bond etched with 40% HF in water to show rutile formation within the glass bonding system; (c) electron backscattered image showing needle growth into the glass bond from the abrasive; (d) devitrified glass bond containing crystals of $\text{Al}_8\text{B}_4\text{O}_{33}$ bounded by two abrasive grains

tends to promote interfacial fracture at the abrasive grain-bond bridge interface. Even if its presence does not cause a reduction in cohesive strength, one method of reducing its effect is for it to form a titanate compound that does not reduce interfacial strength. Examination of fractured high purity aluminum oxide samples revealed preferential etching of the abrasive grain by the glass bond. This is assumed to be dissolution of blocks of β -aluminum oxide ($\text{Na}_2\text{O} \cdot 11\text{Al}_2\text{O}_3$) present in α -aluminum oxide (pure aluminum oxide). The relationship between the wheel wear parameter, grinding ratio, and the firing temperature for vitrified CBN grinding wheel structures containing different amounts of bonding content is shown in Fig. 2.26. An interesting observation one can observe is that the retention of the abrasive grains in the vitrified bonding matrix can be improved by increasing the sintering temperature. In order to investigate the mechanism of CBN retention, samples of the post-fired abrasive structures were polished and etched. Figure 2.27 shows the

Fig. 2.26 Relationship between grinding ratio and firing temperature as a function of bond content for vitrified CBN grinding wheel structures

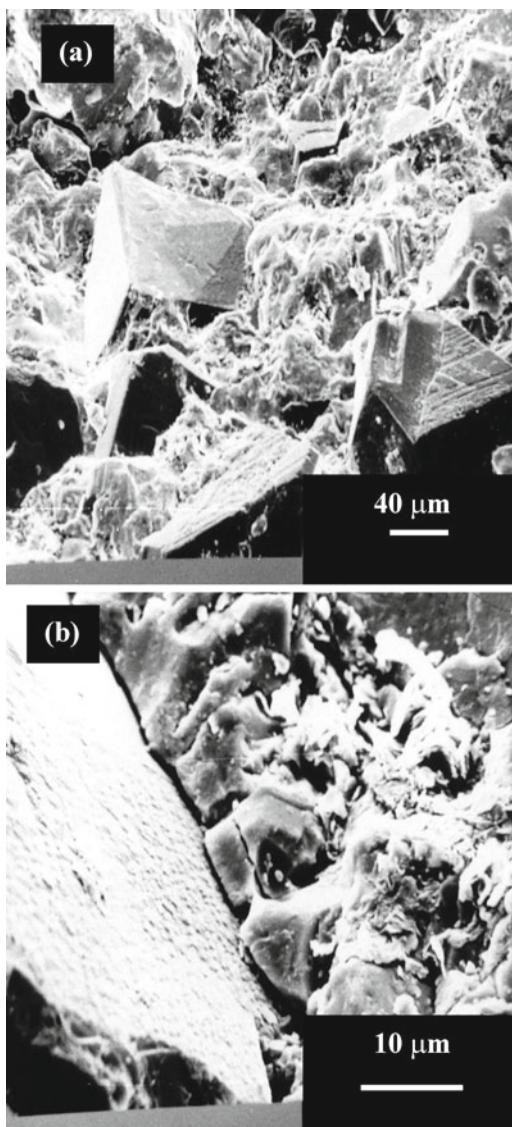


unpolished fracture surfaces of the vitrified CBN grinding wheels. A magnified image of the interface between abrasive grain and bonding bridge is shown in Fig. 2.27b. Interfacial cohesion appears to be quite apparent in this image. Figure 2.28 shows a polished and etched fracture surface in the vicinity of the abrasive grain and bonding bridge. The associated electron probe microanalysis of the image clearly shows a concentration of oxygen at the interface between CBN and glass bonding bridge. The concentration of oxygen appears to be associated with boron and the formation of a boron-containing oxygen layer that separates the alumino-borosilicate bonding system and the CBN abrasive grain. This is thought to be a relatively thin layer of B_2O_3 (boric oxide). As the sintering temperature is increased, the thickness of this layer is also increased with a subsequent loss of boron from the abrasive grain. Figure 2.29 illustrates the relationship between the interfacial layer thickness and sintering temperature. As the temperature is increased further, the width of the interfacial layer tends to stabilize and reaches an equilibrium thickness.

2.3.5 Discussion of Interfacial Compounds on Grinding Wheel Wear

The existence of β -aluminum oxide was established by X-ray methods. When the bond content is low in samples made with high purity aluminum oxide, failure

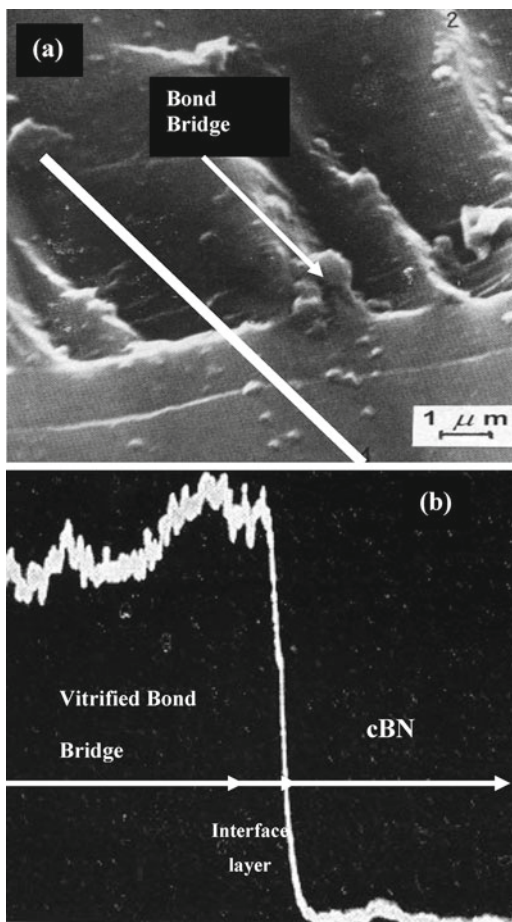
Fig. 2.27 (a) Vitrified CBN grinding wheel structure, (b) interface between CBN abrasive grain and vitrified bonding



occurs by fracture of bonding bridges. At higher bond contents the mode of failure is one of abrasive grain fracture. Fracture at the abrasive grain-bond bridge interface was not observed. This is because the β -aluminum oxide phase is etched away preferentially due to the dissolution of Na_2O into the glass bond that locally increases the fluidity of the bond. This allows the bond to penetrate the surface of the abrasive grain and provides it with enhanced shear resistance.

This effect does not happen with titanium-doped aluminum oxide, in fact, the strength decreases at the softening point of the glass because of enhanced dissolution

Fig. 2.28 (a) Polished cross section of CBN abrasive and bond bridge clearly showing the interface layer, (b) electron probe microanalysis of oxygen across the line scan shown in (a), left-to-right



of aluminum oxide that releases more TiO_2 into the glass bond for rutile needle growth. Therefore, in contrast to Decneut et al. [78], the mode of fracture in titanium-doped structures is interfacial between abrasive grain and glass bond and is not completely dependent on bond content.

Even in the case where bond bridges have preferentially fractured, the mode of fracture is always associated with rutile needle weakening. The vitrification temperature and glass bond content has a significant effect on the elastic modulus of high purity and titanium-doped aluminum oxide structures. The differences in strength between these structures when fired at temperatures above the softening point of the glass bond are due to differences in the crystal structures of the two types of abrasive grain. The presence of β -aluminum oxide in high purity aluminum oxide allows selective dissolution of aluminum oxide to occur that enables stronger bonding to take place between aluminum oxide and glass. This effect does not happen with titanium-doped aluminum oxide where dissolution allows the precipitation

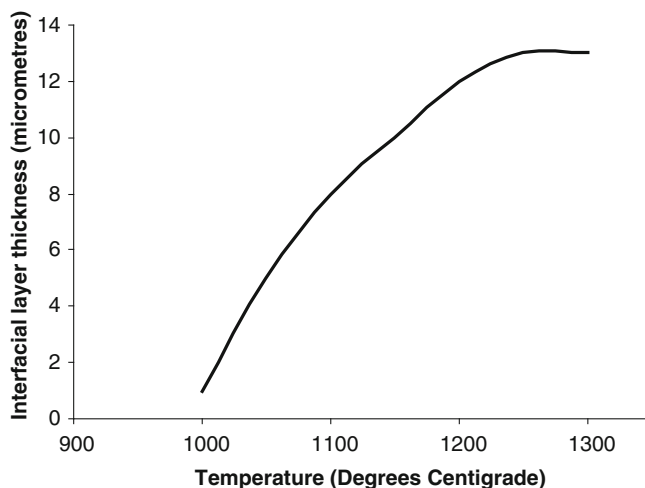


Fig. 2.29 Interfacial layer thickness between CBN and vitrified bonding bridge as a function of sintering temperature

of TiO_2 into the glass bond in the form of rutile needles that reduces the cohesive strength between aluminum oxide and glass.

The existence of an interfacial layer between CBN and glass was thought to be that of the formation of boric oxide (B_2O_3). As sintering continued, the layer became thicker and tended to strengthen the interfacial layer. This is assumed to be the reason why the grinding ratio of the abrasive tool increased as a function of sintering temperature. It was also noted that the size of the CBN grains decreased as sintering temperature increased until an equilibrium interfacial layer thickness was reached. It would also be right to assume that at this point that diffusion of oxygen into the CBN abrasive grain ceases to occur. The fracture surface of the vitrified CBN structure shows that fracture is associated with fracture within the bonding bridge rather than fracture at the CBN–bond bridge interface. This tends to imply that the interfacial bonding layer is stronger than bonding bridge.

2.4 Case Study II: Dissolution of Quartz and Its Effect on Grinding Wheel Wear

When considering individual bond constituents, mineral fluxes and ground glass frits have little direct effect on the ability to manufacture grinding wheels. However, most clay minerals develop some plasticity in the presence of water, which improves the ability to mould the mixture so that the wheel, in its green state, can be mechanically handled [80, 81]. Clays and clay-based fluxes contain an amount of free quartz that has a detrimental effect on the development of strength during vitrification heat treatment. Clays are used to provide vitrified grinding wheels with green strength

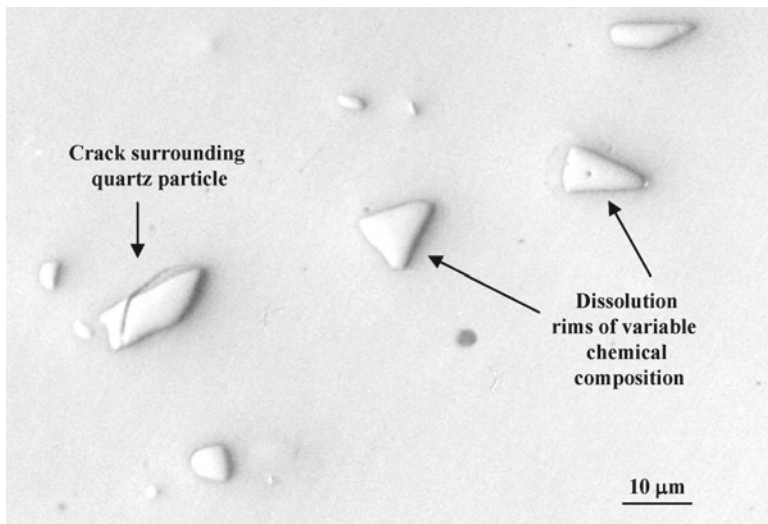


Fig. 2.30 A collection of quartz particles in a vitrified bonding system. The quartz particle on the left has a circumferential crack extending into the dissolution rim and abrasive grain

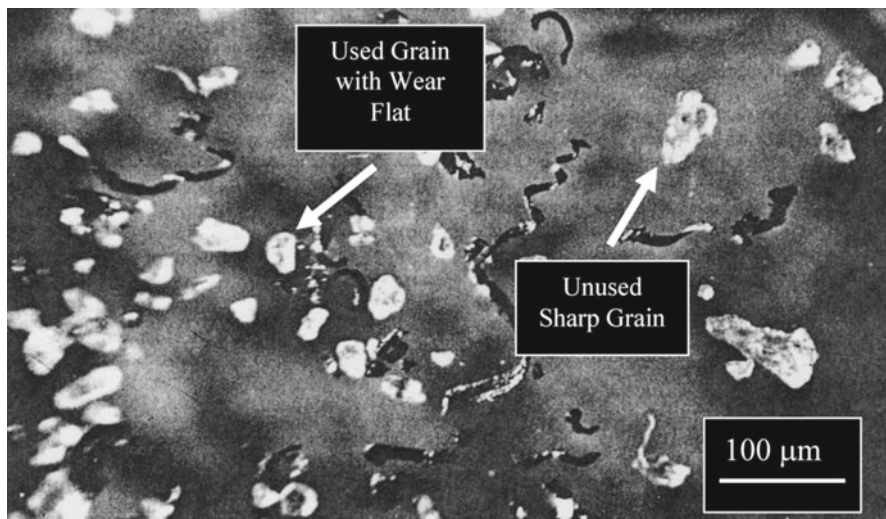


Fig. 2.31 Grinding swarf and a collection of used and unused abrasive cutting grains

during the heat treatment process. However, when the glass material solidifies around the particles of clay and quartz, the displacive transformation of quartz during the cooling stage of vitrification leads to the formation of cracks in the glass around the quartz particle (Fig. 2.30). The strength of the bonding bridge is reduced and leads to the early release of the abrasive particle during the cutting process (Fig. 2.31).

The basic wear mechanisms that affect vitrified grinding wheels are concerned with grain fracture during metal cutting, fracture of bond bridges, mechanical fracture of abrasive grains due to spalling, and fracture at the interface between abrasive grain and bond bridge [82–96]. Failure in vitrified silicon carbide grinding wheels is more probable due to the lack of a well-developed bonding layer between abrasive grain and the glass bond bridge, which is typically only a few micrometers. The lack of adequate bonding is due to the use of a high clay content bonding system with very little opportunity for a glass to form at the interface. High glass content bonding systems tend to aggressively decompose the surface of silicon carbide abrasive grains. In vitrified aluminum oxide grinding wheels, high glass content bonding systems are used extensively and lead to bonding layers in excess of 100 μm in thickness.

In addition to the formation of very thin bonding layers in vitrified silicon carbide grinding wheels, the use of high clay content bonding systems means that there is an increase in the amount of quartz contained in the bond bridges between the abrasive grains. Although the likelihood of decomposition of silicon carbide surfaces is reduced, the probability of bond bridge failure is increased due to the increased quartz content. Therefore, the dissolution of quartz in these bonds is highly desired in order to compensate for a much thinner interfacial bonding layer. Difficulties encountered when developing a dissolution model arise from the fact that the phase boundary between quartz particle and molten glass moves during the diffusion process. The problem of a fixed boundary can be solved without difficulty although this is not equivalent to the conditions associated with a moving boundary between quartz particle and a highly viscous glass melt. The development of dissolution models is required to determine the magnitude of quartz remaining in the bonding system after a period of heat treatment. The models are then compared with experimentally determined quartz content of the bonding systems using X-ray diffraction techniques. Subsequently, dissolution models are used to specify the appropriate heat treatment schedule for a particular bonding system that is used in grinding wheels that grind automotive camshafts and crankshafts depending on the material removal rate and the nature of the material to be ground. The use of X-ray techniques is also applied to measuring phase transformations in grinding wheels that have been subjected to laser irradiation. When using a laser beam to dress the wheel, it is possible to form localized texture in the abrasive grains that allow the grinding wheel to remove material in the superfinishing regime. For the first time, it is reported that grinding wheels are able to provide roughing, finishing, and superfinishing operations in one grinding stroke.

2.4.1 Dissolution Models for Vitrified Grinding Wheel Bonds

When densification occurs in a vitrified grinding wheel after the peak soaking temperature has been reached, the cooling rate is reduced to prevent thermal stress cracking in the bonding layers between abrasive grains. Cooling rates are reduced

when crystalline inversions occur that involve volume changes. The inversion range for quartz and cristobalite is 550–580°C and 200–300°C, respectively. Since the formation of cristobalite is rare in vitrified bonding systems used for grinding wheels, the rapid displacive transformation of quartz tends to promote the formation of cracks in bonding bridges.

When quartz-containing bonds begin to cool from the soaking, or vitrification, temperature it is thought that the liquid phase relieves stresses resulting from the thermal expansion mismatch between itself and the phases, β -quartz, β -cristobalite, and mullite, to at least 800°C. At 800°C, stresses will develop in quartz particles and in the matrix that causes cracking to occur around quartz particles. The shrinkage behavior of quartz and the glass phase has been described by Storch et al. [97]. Between the temperature range, 573 and 800°C, the glass phase shrinks more than the quartz phase that causes tangential tensile stresses to form cracks in the matrix. At 573°C, β -quartz transforms to α -quartz that causes residual stresses around quartz particles to produce circumferential cracking around those same quartz particles (Fig. 2.30). Some of these cracks have been seen to propagate into the glass phase [98]. Similar observations occur in the cristobalite phase. Spontaneous cracking of quartz has been found to occur over a temperature range that depends on the size of the quartz particles [99]. Particles larger than 600 μm diameter cracked spontaneously at 640°C, whereas smaller particles of less than 40 μm diameter cracked at 573°C. This observation agrees with temperature-dependent cracking reported by Kirchhoff et al. [100]. To maintain the integrity of the bond bridges containing coarse quartz particles, the grinding wheel must remain at the vitrification temperature until the quartz particles have dissolved.

The dissolution model assumes that at a constant absolute temperature, T , a particle of quartz melts in the surrounding viscous glass melt and that the rate of change of the volume of quartz present in the melt at a particular instant in time is proportional to the residual volume of quartz. The above assumption is based on the fact that alkali ions diffuse from the viscous glass melt to the boundary of the quartz particle thus producing a dissolution rim around each quartz particle. Diffusion rims around quartz particles are shown in Fig. 2.30.

A high reaction rate will initially occur which continuously decreases as the quartz particle is converted to a viscous melt. Previous models have provided an insight into how various factors contribute to the dissolution of quartz in vitreous bodies. However, Jackson and Mills [101] derived a mathematical relationship that accounts for the change in density when β -quartz transforms to α -quartz on cooling from the vitrification temperature, thus,

$$m_{T,t} = M\gamma \exp\left(-At^{1/2} \exp\left[\frac{-B}{T}\right]\right), \quad (2.2)$$

where, $m_{T,t}$, is the residual mass fraction of quartz at a constant time and temperature couple, M is the original mass fraction of quartz prior to heat treatment, γ is the ratio of densities of β -quartz and α -quartz, A and B are constants, t is time, and T is

Table 2.3 Chemical analyses of raw materials

Oxide (wt%)	China clay	Ball clay	Potash feldspar	Quartz
Al ₂ O ₃	37	31	18.01	0.65
SiO ₂	48	52	66.6	98.4
K ₂ O	1.65	1.8	11.01	0.35
Na ₂ O	0.1	0.2	3.2	0.04
CaO	0.07	0.2	0.09	0.00
MgO	0.03	0.3	0.09	0.00
TiO ₂	0.02	0.9	0.00	0.07
Fe ₂ O ₃	0.68	1.1	0.11	0.03
Loss on ignition	12.5	16.5	0.89	0.20

Table 2.4 Mineralogical analyses of raw materials

Compound (wt%)	China clay	Ball clay	Potash feldspar	Quartz
Quartz	4.05	12.77	4.93	98.40
Orthoclase	0.00	15.23	64.96	0.00
Kaolinite	79.70	62.71	2.17	0.00
Mica	13.94	0.00	0.00	0.00
Soda feldspar	0.8	1.69	27.07	0.00
Miscellaneous oxides/losses	1.51	7.60	0.87	1.60

absolute temperature. The model was compared with experimental data determined using the powder X-ray diffraction method. The experimental work was divided into two parts. The first part concentrates on comparing the dissolution model with X-ray diffraction data using “sintering” bond compositions that are used in vitrified silicon carbide grinding wheels, whilst the second part focuses on comparing the model with “fusible” bond compositions that are used in high-performance vitrified aluminum oxide grinding wheels.

2.4.2 Experimental Procedures

2.4.2.1 Raw Materials and Preparation

The raw materials used in the experimental study (case study 2) were Hymod Prima ball clay, standard porcelain China clay, potash feldspar, and synthetic quartz (supplied as silica flour). The chemical analysis of the raw materials is shown in Table 2.3. Rational analysis of the raw materials was performed to reveal the mineralogical composition of the raw materials. The rational analysis appears in Table 2.4. The bond mixture described is one typically used in vitrified silicon carbide grinding wheels where the erosion of the abrasive grain is reduced by using high clay content bonding systems. This bonding system is used where silicon carbide is predominantly used in grinding cast iron camshafts and crankshafts.

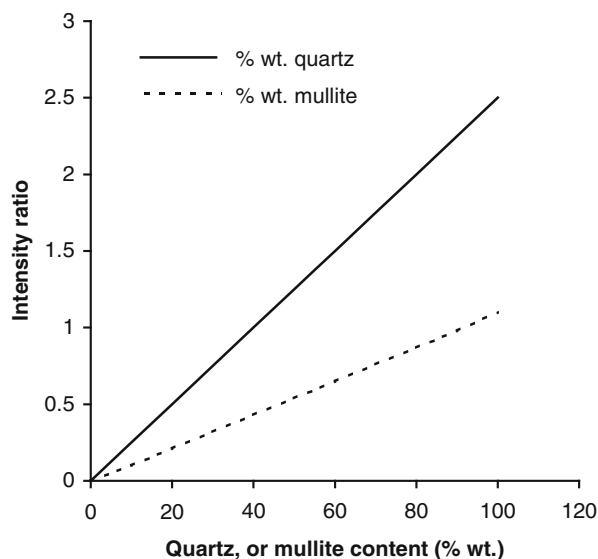
Fusible bonding systems using a mixture of ball clay and potassium-rich feldspar were made to test the model developed by Jackson and Mills [101]. The ball clay used contained 12.77 wt% quartz, and the feldspar contained 4.93 wt% quartz. The bonding system was composed of 66 wt% ball clay and 34% feldspar. The initial quartz content, M , of the bond mixture was 10.1 wt%. The bond mixture described is one typically used in high-performance vitrified aluminum oxide grinding wheels and is used when grinding steel camshafts and crankshafts.

The raw materials were mixed in a mortar, pressed in a mould, and fired at various temperatures. A heating rate of 3°C/min was employed until the vitrification temperature was reached. The typical soaking temperature was varied between 1,200 and 1,400°C for “sintering” bond compositions, and 950 and 1,050°C for “fusible” bond compositions in order to simulate industrial firing conditions. The samples were cooled at a rate of 2°C/min to avoid thermal stress fracture in the bonding bridges between abrasive grains. The fired samples were crushed to form a fine powder in preparation for X-ray diffraction.

2.4.2.2 X-ray Diffraction of Vitrified Bonding Systems

The dissolution model was compared with experimental data using the X-ray powder diffraction method. X-ray diffraction of the raw materials was performed on a Phillips 1710 X-ray generator with a 40 kV tube voltage and a 30 mA current. Monochromatic Cu α radiation, $\lambda=0.154060$ nm, was employed. A scanning speed of 2° per minute for diffraction angles of 2θ was used between 2θ angles of 15° and 60°, and the X-ray intensity was recorded using a computer. The spectrum was then analyzed and compared with known spectra. Powder specimens were prepared by crushing in a mortar and pestle in preparation for quantitative X-ray diffraction. To eliminate the requirement of knowing mass absorption coefficients of ceramic samples for quantitative X-ray diffraction, Alexander and Klug [102] introduced the use of an internal standard. Firstly, the ceramic sample is crushed to form a powder—the sizes of particles should be small enough to make extinction and absorption effects negligible. Secondly, the internal standard to be added should have a mass absorption coefficient at a radiation wavelength such that intensity peaks from the phase(s) being measured are not diminished or amplified. It should be noted that the powder diffraction mixture should be homogeneous on a scale of size smaller than the amount of material exposed to the X-ray beam and was free from preferred orientation. The powder bed that is subjected to “X-rays” should be deep enough to give the maximum diffracted intensity. The expected equilibrium phases from the fired mixtures are quartz (unreacted and partially dissolved), mullite, cristobalite, and glass. However, from the samples tested, the compounds quartz, mullite, and glass were successfully detected. A calibration curve was constructed using a suitable internal standard (calcium fluoride), a diluent, and a synthetic form of the phase(s) to be measured. Synthetic mullite had a purity greater than 99.8%, whilst powdered quartz had a purity greater than 99.84% SiO₂. The method used for quantitative analysis of ceramic powders was developed by Khandelwal and Cook [103].

Fig. 2.32 Calibration curve for quantitative analysis of X-ray determined quartz and mullite using the CaF_2 (111) plane generated by the internal standard



The internal standard provides an intense (111) reflection ($d=0.1354$ nm) lying between the (100) reflection for quartz ($d=0.4257$ nm) and the (200) reflection for mullite ($d=0.3773$ nm). Using $\text{Cu } K\alpha$ radiation ($\lambda=0.15405$ nm), the corresponding values of diffraction angle 2θ are: (100) quartz= 20.82° ; (111) calcium fluoride= 28.3° ; and (200) mullite= 32.26° . Figure 2.32 shows the calibration curve generated by varying proportions of calcium fluoride, synthetic quartz, and mullite. Mass fractions of the crystalline phases in the mixture can be interpreted from the calibration lines by measuring the intensity ratio of the phase(s) to the internal standard. Figure 2.33 shows the diffraction peaks of interest for quantitative analysis lying between 15° and 40° of the diffraction angle 2θ . The figure shows the reflections of the (111) plane of calcium fluoride, (200) plane of mullite, and the (100) plane of quartz. In order to calculate the mass fractions of quartz and mullite in the mixture, the height of the chosen diffraction peak and its width at half-height were measured from the diffraction spectrum. The product of these two measures were then compared with that of the internal standard, and the resultant intensity ratio was used to find the exact mass fraction of the phase(s) measured in the glass that was subjected to X-ray diffraction.

2.4.2.3 Grinding Wheel Performance

A series of grinding wheel experiments were conducted in order to show the difference between bonding systems with different levels of quartz content contained in their bonding bridges. The experiments were conducted using high-speed steels and a high chromium content hypereutectoid steel (AISI 52100) in order to compare with field trials conducted using commercially available vitrified aluminum oxide

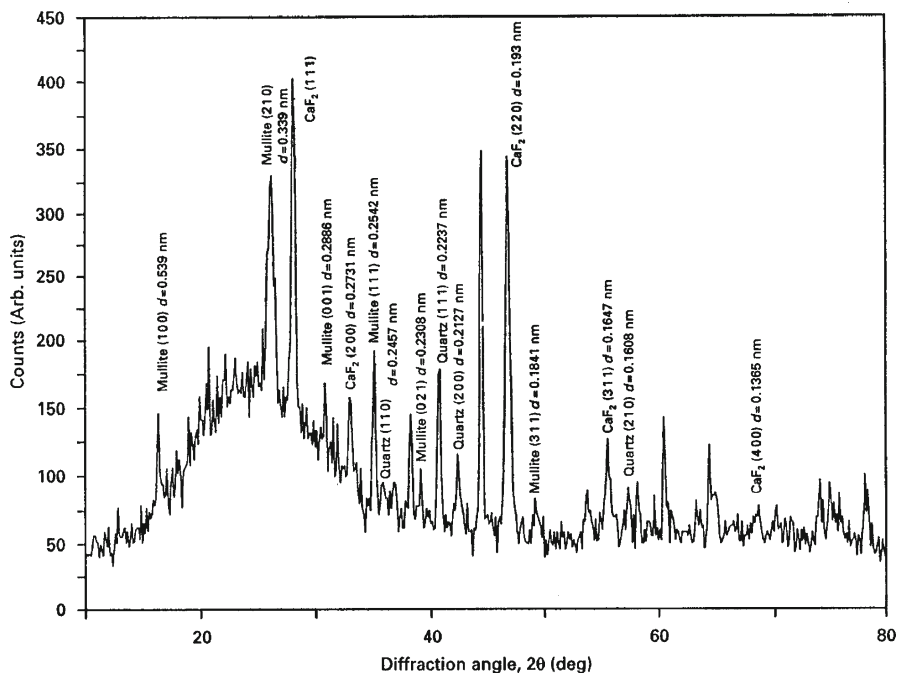


Fig. 2.33 X-ray diffraction spectrum of a vitrified bonding system showing the interplanar distances of crystallographic planes of mullite, quartz, and calcium fluoride. Scan rate was 2° per minute

grinding wheels. A series of controlled experiments were designed to compare grinding wheels under increasing rates of metal removal. The experiments were terminated when a condition of severe burn, chatter, or wheel breakdown was observed. The initial experimental wheels used were: angular white alumina with a low temperature bonding system (wheel specification A); a sol-gel alumina abrasive wheel with angular white abrasive mixed in a one-to-one proportion bonded with a low temperature fired bonding system (wheel specification B); and a monocrystalline alumina wheel with a low temperature fired bonding system (wheel specification C). All wheels were manufactured with a vitreous bond, 60 mesh size abrasive grain (approximately 220 μm in diameter) material, J-hardness grade, and a fairly open structure. Experiments were performed on a Jones and Shipman series ten cylindrical grinding machine using a 450 mm diameter grinding wheel rotating at 33 m/s surface speed. The wheel was dressed using a diamond blade tool using a depth of cut of 30 μm at a feed rate of 0.15 mm/rev, and a final dressing depth of cut of 15 μm prior to grinding workpieces. The amount of material removed was 250 μm per grinding stroke. The coolant flow pressure was 0.5 bar at a flow rate of 15 l/min using a 2% concentrated solution of oil in water.

2.4.3 Experimental Results

2.4.3.1 Silicon Carbide Bonding Systems—Verification and Comparison of Dissolution Models for Quartz

In addition to comparing the experimental results to the dissolution model, results published in the literature were also used to test the accuracy of the model. The composition of the experimental mixtures was matched to those specified by Lundin [81]. Lundin's experimental mixtures were composed of 25 wt% quartz (13.2 μm particle size), 50 wt% clay (kaolin), and 25 wt% flux (potassium feldspar –25 μm average particle size).

The constants A and B for the sintering bonding system were calculated as

$$A = 5.62 \times 10^8, \quad (2.3)$$

$$B = 33374. \quad (2.4)$$

From which the experimental activation energy, Q , is 132.65 kcal/mol. The residual quartz content for the sintering bonding system is given as follows:

$$m_{T,t} = 26.25 \cdot \exp \left[-5.62 \times 10^8 \cdot t^{1/2} \cdot e^{-33,374/T} \right]. \quad (2.5)$$

The data comparing Lundin's experimental results, the author's experimental results, and the dissolution model is shown in Table 2.5. When the data is plotted as the logarithm of $(-\ln[m/M]/t^{1/2})$ versus the reciprocal of absolute temperature, $1/T$, then all data fits a straight-line relationship. The gradient was calculated to be 33,374, the constant B , using two data points. Lundin's experimental gradient gave a value of 32,962 using the least squares method, and 34,000 for the present work. The corresponding activation energies for both systems are 131 kcal/mol for Lundin's work [81] and 135 kcal/mol for the present work, respectively. Figures 2.34 and 2.35 show the effects of time on residual quartz content at different temperatures according to (2.5) together with comparative experimental data.

A comparison was made with dissolution models published in the literature. One of the earliest models was derived by Jander [104]. The equation can be expressed as

$$\left(1 - \sqrt[3]{1 - Z}\right)^2 = \left\{ \frac{C_1 \cdot D}{r^2} \right\} \cdot t, \quad (2.6)$$

where Z is the volume of quartz that has been dissolved, r is the original particle radius, and D is the diffusion coefficient for the diffusing species. This equation can be transformed into mass fractions using Archimedes' law, thus,

$$\left(1 - \sqrt[3]{\frac{m}{M}}\right)^2 = C_2 \cdot t, \quad (2.7)$$

Table 2.5 Residual quartz content of a sintering bonding system at various vitrification temperatures

Temperature (°C)	Time (h)	Lundin's experimental result (wt%)	Experimental result (wt%)	Jackson and Mills' [101] result (wt%)
1,200 (1,473 K)	1	24.1	24.2	24.2
1,200	1	24.7	24.3	24.2
1,200	1	26.1	24.8	24.2
1,200	2	23.7	23.8	23.4
1,200	2	23.6	23.9	23.4
1,200*	2	23.4	23.4	23.4
1,200	4	21.3	22.2	22.3
1,200	8	20.3	20.9	20.8
1,200	18	19.0	18.5	18.6
1,200	18	18.9	18.6	18.6
1,200	48	15.2	15.1	14.9
1,250 (1,523 K)	1	22.7	22	22.1
1,250*	2	20.6	20.6	20.6
1,250	4	18	18.5	18.6
1,250	8	15.5	16	16.2
1,250	18	12.6	12.5	12.6
1,250	48	8.3	7.8	8.0
1,300 (1,573 K)	0.5	22.6	20.4	20.6
1,300	0.5	21	20.9	20.6
1,300	1	20	18.3	18.6
1,300	2	16.1	15.9	16.2
1,300	4	13.4	12.8	13.2
1,300	8	10	9.7	9.9
1,300	18	5.9	5.8	6.1
1,300	50	1.6	1.8	2.3
1,300	120	0.3	0.2	0.6

Lundin's [81] experimental data is compared with the author's experimental data and the model [101]. The *asterisk* indicates that the values used for deriving the constants are used in the theoretical model

where, C is a constant dependent on soaking temperature and initial particle size of quartz. Krause and Keetman [105] expressed the dissolution of quartz as a function of isothermal firing time, viz,

$$M - m = C_3 \cdot \ln t, \quad (2.8)$$

where M is the initial quartz content, m is the residual quartz content after time, t . The unit of time here is seconds such that after 1 s of firing the residual quartz content is equal to the initial quartz content. Monshi's dissolution model [106] can be transformed into the following equation assuming isothermal firing conditions

$$\ln \left\{ \frac{m}{M} \right\} = -C_6 \sqrt{t}. \quad (2.9)$$

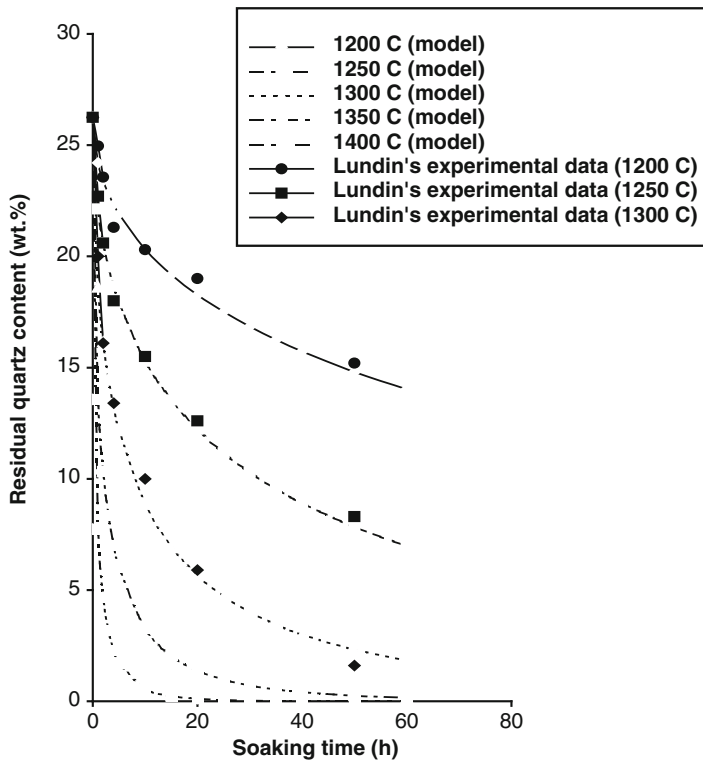


Fig. 2.34 Effect of time on residual quartz content of a sintering bonding system according to Jackson and Mills model [101] and compared with Lundin's experimental data [81]

Jackson and Mills' model [108] for isothermal firing conditions is transformed into

$$\ln \left\{ \frac{m}{\gamma \cdot M} \right\} = -C_{\gamma} \sqrt{t}, \quad (2.10)$$

where γ is the ratio of densities of β - and α -quartz. Constants for all the equations presented here are calculated using quartz mass fraction data after 18 h firing. The constants are dimensioned in seconds. The equations shown were compared with experimental data generated by Lundin [81] for a clay-based material containing 40 wt% kaolin, 40 wt% quartz, and 20 wt% feldspar. According to the transformed equations, the mass fraction of quartz can be calculated as follows:

Jander's model [104]

$$m = 41.9 \cdot \left(1 - \left\{ 1.55 \times 10^{-6} \cdot t \right\} \right)^{3/2}. \quad (2.11)$$

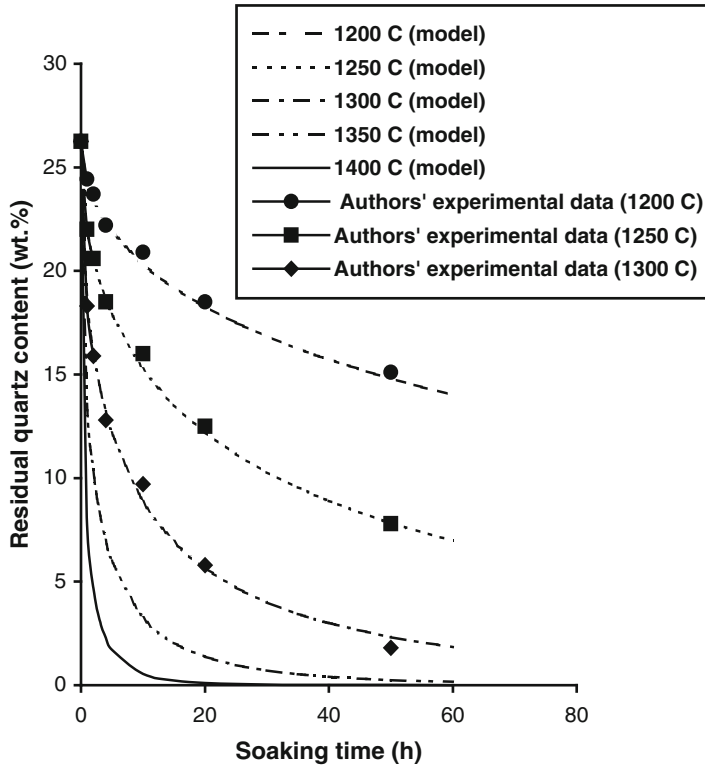


Fig. 2.35 Effect of time on residual quartz content of a sintering bonding system according to Jackson and Mills' model [101] and compared with the authors' experimental data

Krause and Keetman's model [105]

$$m = 41.9 - (2.58 \cdot \ln t) \quad (2.12)$$

Monshi's model [106]

$$m = 41.9 \cdot e^{-4.5 \times 10^{-3} \sqrt{t}} \quad (2.13)$$

Jackson and Mills' model [101]

$$m = 41.73 \cdot e^{-4.5 \times 10^{-3} \sqrt{t}} \quad (2.14)$$

The transformed equations are then tested using data provided by Lundin [81]. Referring to Table 2.6, it can be shown that the mass fraction of quartz obtained using the equations derived by Jander [104] and Krause and Keetman [105] did not agree with Lundin's experimental results [81]. The results obtained using Monshi's model [106] are in much better agreement compared to Lundin's data.

However, the results obtained using Jackson and Mills' model [101] are more accurate at predicting the mass fraction of quartz remaining owing to the differences

Table 2.6 Residual quartz content for different soaking times at 1,300°C for a sintering bonding system composed of 40 wt% kaolin, 40 wt% quartz, and 20 wt% feldspar (Lundin's mixture number M21 [81]) compared with other dissolution models

Time (h)	Lundin's experimental data [81]	Jander [104]	Krause and Keetman [105]	Monshi [106]	Jackson and Mills [101]
0	41.9	41.9	0.00	41.9	41.9
0.5	35.9	41.72	22.55	34.61	34.76
1	32.8	41.54	20.76	31.97	32.12
2	29.2	41.19	18.97	28.58	28.72
4	23.2	40.49	17.18	24.39	24.51
8	19.5	39.11	15.39	19.49	19.59
18	13.3	35.72	13.30	13.30	13.36
24	10.7	33.74	12.56	11.13	11.19
48	6.9	26.18	10.77	6.43	6.51
120	3.6	7.85	8.96	2.17	2.17
190	2.7	0.00	7.22	1.00	1.01
258	2.0	0.00	6.43	0.54	0.55

in the density of quartz. After long periods of heat treatment, the model predicts lower magnitudes of mass fractions of quartz when compared to Lundin's experimental results [81].

2.4.3.2 Aluminum Oxide Bonding Systems—Verification and Comparison of Dissolution Models for Quartz

The constants, A and B , for the fusible bonding system were determined using time and temperature couples at 2 and 10 h and were calculated to be, -5.2×10^8 and $-33,205$, respectively. The dissolution equation then becomes

$$m_{T,t} = 10.06 \exp \left[-5.2 \times 10^8 t^{1/2} \cdot e^{-33,205/T} \right]. \quad (2.15)$$

Equation (2.15) is used to compare the experimentally determined mass fraction of quartz remaining after heat treatment with the predicted values. The calculated mass fraction of quartz remaining after a period of heat treatment is calculated using the equation derived by Jackson and Mills [101]. The results of the dissolution model compare well with the experimental data over short periods of time. However, over longer periods of heat treatment the model tends to become less accurate (Fig. 2.36). A comparison was made with published dissolution models. The equations shown were compared with experimental data at 1,050°C. According to the transformed equations, the mass fraction of quartz can be calculated as follows:

Jander's model [104]

$$m = 10.1 \cdot \left(1 - \left\{ 3.44 \times 10^{-6} \cdot t \right\}^{3/2} \right). \quad (2.16)$$

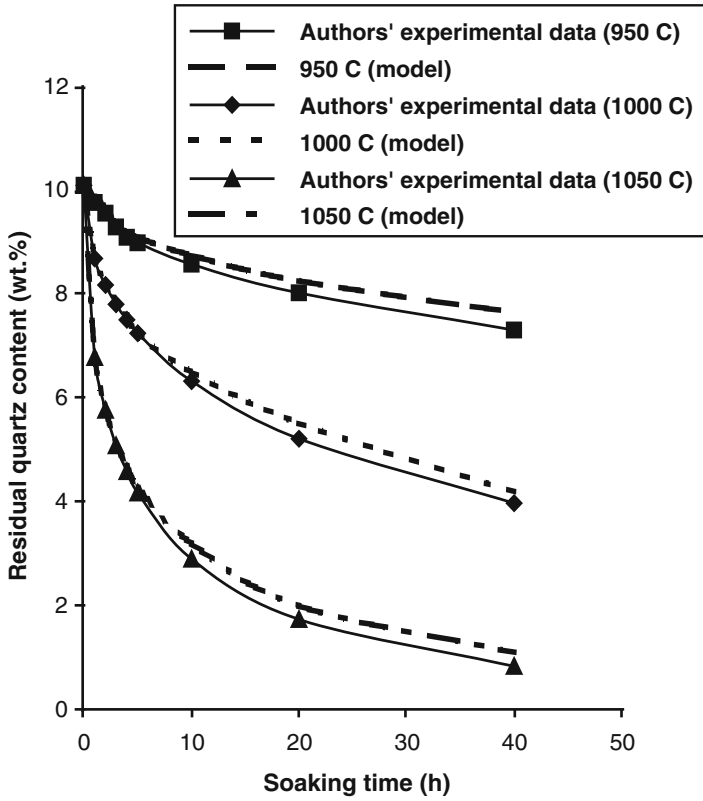


Fig. 2.36 Effect of time on residual quartz content of a fusible bonding system according to Jackson and Mills' model [81] and compared with the author's experimental data

Krause and Keetman's model [105]

$$m = 10.1 - (0.59 \cdot \ln t). \quad (2.17)$$

Monshi's model [106]

$$m = 10.1 \cdot e^{-6.4 \times 10^{-3} \sqrt{t}}. \quad (2.18)$$

Jackson and Mills' model [81]

$$m = 10.06 \cdot e^{-6.37 \times 10^{-3} \sqrt{t}}. \quad (2.19)$$

Table 2.7 Residual quartz content for different soaking times at 1,050°C for a fusible bonding system compared with other dissolution models

Time (h)	Experimental data	Jander model [104]	Krause and Keetman model [105]	Monshi's model [106]	Jackson and Mills' model [81]
0	10.1	10.1	0	10.1	10.1
1	6.84	9.91	5.23	6.88	6.86
2	5.79	9.72	4.82	5.87	5.86
3	5.13	9.54	4.58	5.21	5.19
4	4.7	9.36	4.41	4.7	4.68
5	4.28	9.18	4.28	4.28	4.28
10	3.2	8.28	3.87	2.99	3
20	2	6.6	3.46	1.81	1.82
40	1.1	3.62	3.04	0.89	0.89

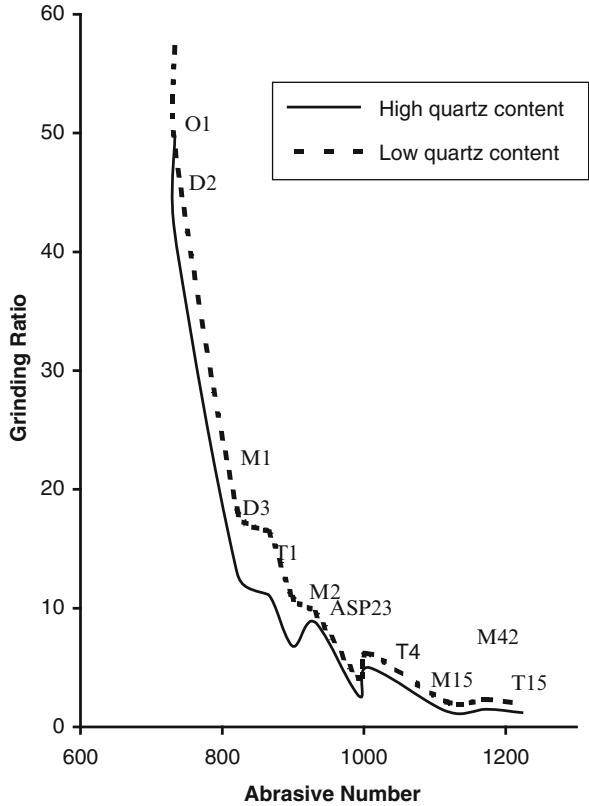
With reference to Table 2.7, it can be shown that the mass fraction of quartz obtained using the equations derived by Jander [104] and Krause and Keetman [105] did not agree with the experimental results at 1,050°C. The results obtained using Monshi's model [106] are in much better agreement compared to the experimental data. However, the results obtained from Jackson and Mills' model are more accurate at predicting the mass fraction of quartz remaining owing to the differences in the density of quartz. After long periods of heat treatment, the model predicts slightly lower magnitudes of mass fractions of quartz when compared to the experimental results. The use of X-rays to predict the level of quartz in vitrified bonding systems can be used to specifically design grinding wheels for specific grinding processes where the quartz content in the bonding system will reduce the economic impact of using vitrified alumina grinding wheels.

2.4.3.3 Grinding Wheel Experiments

The dissolution of quartz during heat treatment has a significant effect on the wear of vitrified grinding wheels. Figure 2.37 shows the effect of using a high- and a low-quartz content bonding system on the wear of vitrified aluminum oxide grinding wheels grinding a large number of tool steel materials [107]. The classification of tool steels is in the form of an abrasive hardness number, which is a weighted average of the number of carbides contained within the tool material. As shown in Fig. 2.37, the grinding ratio, or G-ratio, is a measure of the efficiency of the grinding wheel. It is the quotient of the volume of workpiece material removed and the volume of the wheel material removed. The figure demonstrates the effectiveness of reducing the quartz content of the bonding system. X-ray diffraction techniques have been used to characterize the bonding system and is an effective method in the selection of raw materials used for high efficiency grinding wheels.

Further experimental results using hypereutectoid steels were compared with field experiments using camshaft and crankshaft grinding operations as the basis for comparison. Forty workpiece samples were ground and the results of the initial

Fig. 2.37 Effect of the abrasive number on the grinding ratio for a high-quartz content and a low-quartz content bonding system grinding tool steel materials in the cylindrical surface grinding mode. Tool steel material is marked on the trend lines and is a function of the carbide content in their microstructure expressed as an abrasive number



experiments are shown in Figs. 2.38, 2.39, and 2.40. None of the wheels used produced chatter vibrations or burned the workpieces, which was represented by a change in the level of grinding power. The grinding wheels gave a similar performance level, surface roughness, and grinding ratio. At low grinding rates, it was possible to differentiate between the grinding performance of each wheel.

The sol-gel wheel gave the best performance in terms of surface roughness and the highest grinding ratio whilst the angular white alumina wheel provided the worst results that resulted in rapid wheel wear. The use of monocrystalline abrasives at moderate metal removal rates ground approximately 30 workpiece materials before it started to breakdown. From these initial results, it can be shown that sol-gel abrasive wheels operate well at high power levels and can grind more efficiently at higher metal removal rates compared to angular white and monocrystalline abrasive grinding wheels. At low metal removal rates, there appears to be no significant difference between the grinding wheels used in the experiments. These experiments also show that bonding systems that are rich or depleted in quartz particles have a significant effect on the breakdown of the grinding wheel during grinding experiments—a significant factor in the subsequent change in grinding ratio.

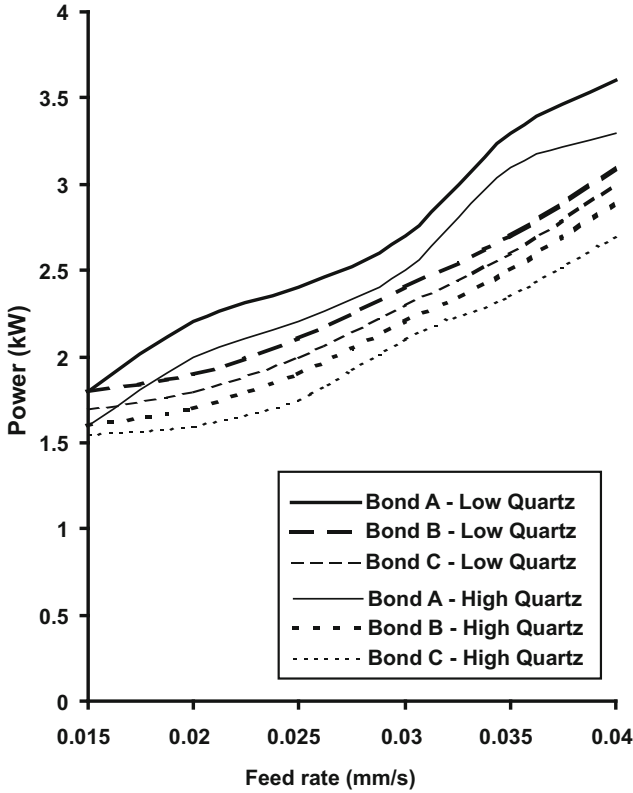


Fig. 2.38 Grinding power as a function of feed rate for vitrified aluminum oxide grinding wheels with different types of abrasive and bond. Grinding conditions: wheel surface speed=33 m/s; depth of cut=0.25 mm; dress conditions=diamond blade traversed at 0.15 mm/rev at a depth of cut of 0.03 mm

2.5 Discussion

A model describing the dissolution of quartz has been used to predict the mass fraction of quartz remaining after a period of heat treatment in vitrified grinding wheel bonding systems. The model has been compared with experimentally determined mass fractions of quartz in an industrial vitrified bonding system. However, the assumptions made when formulating the model may invalidate its wider application. In diffusion-controlled processes, the total flux per unit time is proportional to the total surface area available and the concentration gradient at the interface between quartz particle and viscous melt. The model assumes that a linear concentration gradient exists across the spherical shell of reaction products that invalidates the real situation where quartz particles are anything but perfect spheres.

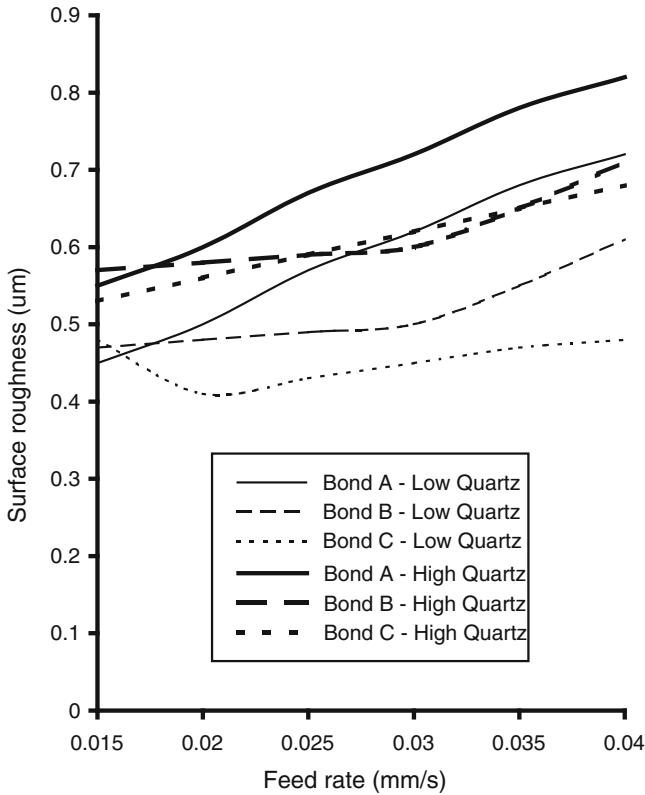


Fig. 2.39 Surface roughness as a function of feed rate for vitrified aluminum oxide grinding wheels with different types of abrasive and bond. Grinding conditions: wheel surface speed = 33 m/s; depth of cut = 0.25 mm; dress conditions = diamond blade traversed at 0.15 mm/rev at a depth of cut of 0.03 mm

The model does obey the parabolic law for diffusion around a sphere that can only apply when the sphere has a very low solubility in the solvent. However, this is not the case for quartz in most silicate systems. Also, the bonding between quartz particle and viscous glass melt is moving and not stationary. This implies that the concentration gradient is transient and not constant. The experimental data used to justify the accuracy of the dissolution model do not meet the conditions implicit in the model. The reactions between the three basic components of the bonding system, i.e., clay, feldspar, and quartz, cannot solely be described as diffusion-controlled dissolution of quartz in a liquid phase of constant composition and properties. It seems unlikely that the model can predict the mass fraction of quartz in any silicate system with great accuracy. However, over short soaking periods at the vitrification temperature, the results of the model compare well with experimental data.

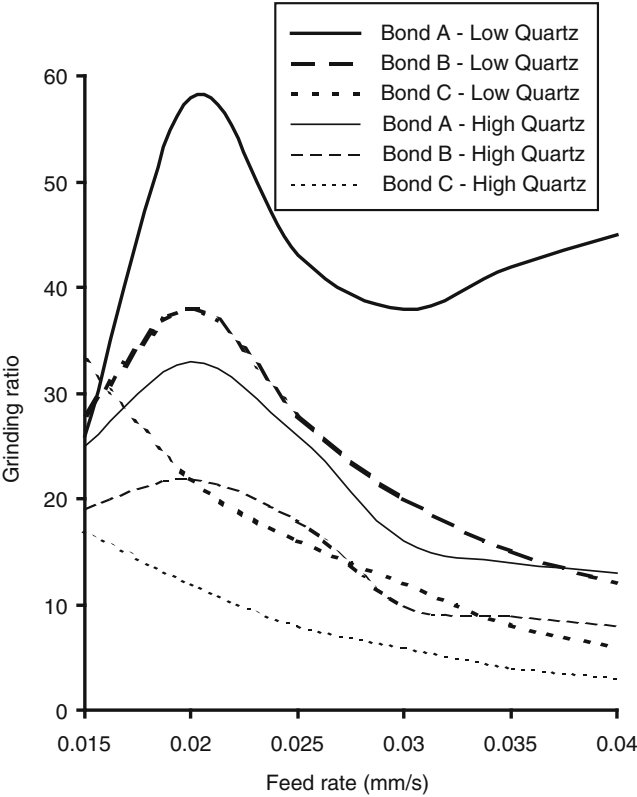


Fig. 2.40 Grinding ratio as a function of feed rate for vitrified aluminum oxide grinding wheels with different types of abrasive and bond. Grinding conditions: wheel surface speed=33 m/s; depth of cut=0.25 mm; dress conditions=diamond blade traversed at 0.15 mm/rev at a depth of cut of 0.03 mm

X-ray diffraction methods can be used to identify planes in vitrified bonding systems during and after heat treatment, which can be used to determine the correct bond formulations for grinding wheels used in specific applications. The experimental results show that bonds with high-quartz contents lead to much lower grinding ratios and surface roughness levels. This implies that X-ray methods can be used to increase the economic productivity of using such tools.

High Performance Grinding and Advanced Cutting Tools

Jackson, M.J.; Hitchiner, M.P.

2013, VIII, 100 p. 83 illus., 16 illus. in color., Softcover

ISBN: 978-1-4614-3115-2